

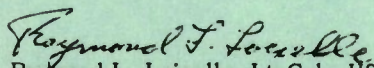
The work reported in this document was performed at Lincoln Laboratory, a center for research operated by Massachusetts Institute of Technology, with the support of the Department of the Air Force under Contract F19628-78-C-0002.

This report may be reproduced to satisfy needs of U.S. Government agencies.

The views and conclusions contained in this document are those of the contractor and should not be interpreted as necessarily representing the official policies, either expressed or implied, of the United States Government.

This technical report has been reviewed and is approved for publication.

FOR THE COMMANDER


Raymond L. Loiselle, Lt. Col., USAF
Chief, ESD Lincoln Laboratory Project Office

Non-Lincoln Recipients

PLEASE DO NOT RETURN

Permission is given to destroy this document
when it is no longer needed.

MASSACHUSETTS INSTITUTE OF TECHNOLOGY
LINCOLN LABORATORY

SOLID STATE RESEARCH

QUARTERLY TECHNICAL SUMMARY REPORT

1 AUGUST - 31 OCTOBER 1977

ISSUED 25 JANUARY 1978

Approved for public release; distribution unlimited.

LEXINGTON

MASSACHUSETTS

ABSTRACT

This report covers in detail the solid state research work of the Solid State Division at Lincoln Laboratory for the period 1 August through 31 October 1977. The topics covered are Solid State Device Research, Quantum Electronics, Materials Research, Microelectronics, and Surface-Wave Technology. Funding is primarily provided by the Air Force, with additional support provided by the Army, ARPA, NSF, and DOE.

CONTENTS

Abstract	iii
Introduction	vii
Reports on Solid State Research	x
Organization	xiv
 I. SOLID STATE DEVICE RESEARCH	 1
A. GaInAsP/InP Avalanche Photodiodes	1
B. Epitaxial Homostructure $\text{Pb}_{1-x}\text{Sn}_x\text{Te}$ Diode Lasers with CW Operation Up to 100 K	3
C. High-Resistivity Layers in n-InP Produced by Fe-Ion Implantation	7
D. Post-to-Pad Indium-to-Indium Lead Bonding	11
 II. QUANTUM ELECTRONICS	 15
A. Operating Characteristics of a $\text{MgF}_2\text{:Ni}$ Laser	15
B. Mini-TEA CO_2 Laser	18
C. Nonlinear Infrared Processes in Cryogenic Liquids	19
D. Collisionless Intramolecular Energy Transfer in Vibrationally Excited SF_6	21
 III. MATERIALS RESEARCH	 25
A. Simplified Fabrication of GaAs Homojunction Solar Cells with Increased Conversion Efficiencies	25
B. Chemisorbed Phases of O_2 on TiO_2 and SrTiO_3	27
 IV. MICROELECTRONICS	 33
A. Quasi-optical Mixers at Submillimeter Wavelengths	33
1. Fundamental Waveguide Mixer	33
2. Line Source in a Corner Reflector	35
B. Charge-Coupled Devices: SAW/CCD Buffer Memory	37
C. Charge-Coupled Devices: Imagers	39
D. Charge-Coupled Devices: Programmable Transversal Filter	43
E. Wafer-Processing Techniques for Minimum Dark Current	46
 V. SURFACE-WAVE TECHNOLOGY	 49
A. Precision SAW Fourier-Transform System	49
B. Propagation Modes in Gap-Coupled Acoustoelectric Devices	53
C. Acoustoelectric Integrating Correlator	57

INTRODUCTION

I. SOLID STATE DEVICE RESEARCH

High-speed gains of up to 12 have been achieved in the 1.15- to 1.25- μm wavelength range with avalanche photodiodes of the quaternary alloy GaInAsP. The low-bias quantum efficiency at 1.15 μm was approximately 45 percent. When biased to yield a gain of about 8, the risetime of the avalanche diode response to a pulse from a GaInAsP/InP laser was less than 200 psec.

CW operation of epitaxially grown $\text{Pb}_{1-x}\text{Sn}_x\text{Te}$ homostructure diode lasers has been achieved for heat-sink temperatures up to 100 K. Relatively large output powers are observed for the $x = 0$ devices, the maximum obtained being 4.5-mW single-ended output from a LPE homostructure at ~ 15 K.

The ion implantation of Fe in n-type InP yields high-resistivity layers with $\rho \geq 10^7 \Omega\text{-cm}$. Some diffusion of the implanted Fe occurs during the post-implantation anneal, with the effect being more pronounced on samples implanted at room temperature than in samples implanted at 200°C.

A high-yield, good-reliability bonding technique has been developed which allows leads to be bonded to small bonding pads on fragile semiconductor materials. The technique provides a simple means of attaching leads to soft crystals without apparent damage, and has allowed 12-element arrays of GHz-bandwidth HgCdTe heterodyne receivers to be fabricated.

II. QUANTUM ELECTRONICS

A $\text{MgF}_2\text{:Ni}$ laser at 35 K has been operated in the 1.6- to 1.7- μm region, with 1.7 W of CW output power, an absorbed pump power conversion efficiency of 37 percent, and an absorbed pump power threshold of 50 mW. Damped relaxation oscillations leading to true CW operation and lasing up to a crystal temperature of 200 K have been observed.

A mini-TEA CO_2 laser has operated at pulse-repetition rates up to 40 Hz and at pulse output levels to 44 mJ. The laser has been used for frequency doubling by pumping CdGeAs_2 crystals, achieving an average pulse-energy conversion efficiency of 18 percent.

Efficient four-wave sum-and-difference frequency generation of the outputs of two CO_2 TEA lasers has been observed in liquid CO-O_2 mixtures at 77 K. The potential for efficient frequency tripling of CO_2 laser radiation in SF_6 dissolved in liquid argon has also been examined.

Double-resonance measurements using CO_2 laser excitation have been used to provide evidence for collisionless intramolecular energy transfer in vibrationally excited SF_6 . An intramolecular energy transfer time of $3 \pm 1 \mu\text{sec}$ is inferred for an excess energy of three quanta in the ν_3 mode.

III. MATERIALS RESEARCH

Conversion efficiencies as high as 20 percent have been obtained for single-crystal GaAs shallow-homojunction cells without $\text{Ga}_{1-x}\text{Al}_x\text{As}$ layers. These cells, which are fabricated by a simplified technique that does not require any vacuum processing steps, utilize an $n^+/p/p^+$ structure with an antireflection coating prepared by anodic oxidation of the n^+ layer.

Ultraviolet photoemission spectroscopy has been used to investigate the chemisorption of O_2 on various surfaces of TiO_2 and SrTiO_3 , two materials that catalyze the decomposition of water into H_2 and O_2 by photoelectrolysis. Several adsorbed phases are formed; the same initial phase, which is believed to consist of O^{2-} ions, is present on all surfaces for low O_2 exposures.

IV. MICROELECTRONICS

Two approaches are being pursued to build a quasi-optical mixer at submillimeter wavelengths to replace the more conventional approach of embedding a diode in a fundamental waveguide. The first approach is to modify the standard overmoded waveguide diode-wafer package by making a fundamental waveguide insert for use with the package. The second approach uses a long traveling-wave line source set in a corner reflector. Both configurations are being modeled at X-band and are also under construction for submillimeter operation.

An integrated buffer memory having a surface-acoustic-wave (SAW) input and a charge-coupled-device (CCD) output has been designed and is being fabricated. Initial work is being done with a 3.56- μsec -long acoustoelectric interaction region operating at a 100-MHz center frequency with about a 30-MHz bandwidth. The cell size of the CCD has been chosen based on the need to have an effective sampling frequency, which is directly related to cell size, that is sufficiently high to avoid aliasing but not so high that it overlaps the input spectrum.

Fabrication of the 100- \times 400-element CCD imager has continued, and yields based on static testing have averaged 14 percent in recent runs. Dynamic test yields have been somewhat lower due to processing problems which have been corrected. Transfer inefficiencies of 2×10^{-5} and dark currents of 4 nA/cm² in the output register have been measured. Single devices have been packaged and operated as imagers in the stare-and-integrate mode in anticipation of evaluating them on the telescope at the GEODSS experimental test system near Socorro, New Mexico.

A test device consisting of an MOS shift register and latch circuits has been made to demonstrate the feasibility of fabricating high-performance n-channel MOS logic devices which are part of a programmable transversal filter that is being developed. The processing techniques are compatible with fabricating the high-speed CCD portion of this device. The shift register has been operated at 8 MHz and as slow as 666 Hz with a high-state output of 10 V. The device has been operated as a true static shift register, and it has been established that a digital reference can be stored in the static latch circuits while a new reference is loaded into the shift register.

Dark current in buried-channel CCDs results from heavy metal contaminants such as gold which are present in unprocessed wafers and are also introduced from the wafer-processing environment. The use of the gettering effect of a high-concentration ($>10^{19} \text{ cm}^{-3}$) phosphorous diffusion into the wafer back side, the so-called POGO (pre-oxidation gettering of the other side) process, along with the protection of an oxide layer, has reduced gold trap densities to less than $2 \times 10^{10} \text{ cm}^{-3}$ and the dark current in gate-controlled diodes to less than 1 nA/cm^2 .

V. SURFACE-WAVE TECHNOLOGY

The precise linear FM response which can be obtained from reflective-array compressors has made possible the realization of large-bandwidth Fourier-transform systems using surface-wave devices. Such systems offer the potential advantages of high speed combined with smaller size and less power consumption than equivalent digital systems. A 300-point Fourier-transform system with a bandwidth of 10 MHz has been breadboarded for the first phase of the demonstration of the performance of this analog approach. The system is designed for a combination of high precision and wide dynamic range in the Fourier transform.

In gap-coupled acoustoelectric SAW devices, the silicon strip held in close proximity to the surface of the LiNbO_3 delay line weakly guides the surface wave and forms an overmoded waveguide. The properties of the modes are modified by the support structure (typically ion-etched posts or rails) which spaces the silicon from the LiNbO_3 surface. The resulting coupling and scattering out of the waveguide cause excess loss in acoustoelectric devices. The propagation characteristics of surface waves in delay lines having various types of support structures have been measured by electrostatic and optical probes. The measured mode behavior agrees with a theoretical model, and this understanding has led to modified geometries which yield improved device response.

Encouraging results have been obtained with the acoustoelectric Schottky-diode/ LiNbO_3 integrating correlator. Good linearity of the integration process has been achieved in correlating biphasic modulated codes with $4 \mu\text{sec}$ chip length and up to 10 msec duration. In these tests, the desired signal was intentionally added to a high-level pseudonoise interference signal, thereby demonstrating a signal-processing gain of 34 dB in the presence of a strong jammer. Long-storage-time diode arrays and application of a reverse bias on the array are essential to linearizing the integration process.

REPORTS ON SOLID STATE RESEARCH

15 August through 15 November 1977

PUBLISHED REPORTS

Journal Articles

JA No.

4694	X-Ray Photoemission Spectroscopy Studies of Sn-Doped Indium-Oxide Films	J. C. C. Fan J. B. Goodenough*	J. Appl. Phys. <u>48</u> , 3524 (1977)
4736	New C.C.D. Programmable Transversal Filter	B. E. Burke W. T. Lindley	Electron. Lett. <u>13</u> , 521 (1977)
4738	Analysis of the 4- μ m $\nu_1 + \nu_3$ Combination Band of SO ₂	A. S. Pine G. Dresselhaus B. Palm R. W. Davies* S. A. Clough*	J. Mol. Spectrosc. <u>67</u> , 386 (1977)
4744	Vibrational Two-Photon Resonance Linewidths in Liquid Media	S. R. J. Brueck	Chem. Phys. Lett. <u>50</u> , 516 (1977)
4745	Proton Bombardment in InP	J. P. Donnelly C. E. Hurwitz	Solid-State Electron. <u>20</u> , 727 (1977)
4748	310-MHz SAW Resonator with Q at the Material Limit	R. C. M. Li	Appl. Phys. Lett. <u>31</u> , 407 (1977)
4751	Vibrational Energy Relaxation of CH ₃ F Dissolved in Liquid O ₂ and Ar	S. R. J. Brueck T. F. Deutsch R. M. Osgood, Jr.	Chem. Phys. Lett. <u>51</u> , 339 (1977)
4752	Ion-Implanted n- and p-Type Layers in InP	J. P. Donnelly C. E. Hurwitz	Appl. Phys. Lett. <u>31</u> , 418 (1977)
4757	High-Efficiency GaAs Shallow-Homojunction Solar Cells	C. O. Bozler J. C. C. Fan	Appl. Phys. Lett. <u>31</u> , 629 (1977)
4761	High-Sensitivity Infrared Heterodyne Radiometer Using a Tunable-Diode-Laser Local Oscillator	R. T. Ku D. L. Spears	Opt. Lett. <u>1</u> , 84 (1977)
4766	A New Interferometric Alignment Technique	D. C. Flanders H. I. Smith S. Austin*	Appl. Phys. Lett. <u>31</u> , 426 (1977)
4773	Suppression of Bulk-Scattering Loss at S.A.W.-Resonator Reflectors	R. C. M. Li J. A. Alusow	Electron. Lett. <u>13</u> , 580 (1977)

* Author not at Lincoln Laboratory.

Meeting Speeches

MS No.

- | | | | |
|-------|---|------------------------------|--|
| 4109 | Solar Energy Application
of Natural Zeolites | D. I. Tchernev | Proc. 2nd Workshop on the
Use of Solar Energy for the
Cooling of Buildings, Uni-
versity of California, Los
Angeles, 4-6 August 1975,
edited by F. and J. W.
de Winter (July 1976),
pp. 307-319 |
| 4362A | Surface State Studies on SrTiO ₃
Electrodes | J. G. Mavroides | In <u>Semiconductor Liquid-
Junction Solar Cells</u> , edited
by A. Heller, Proceedings
Vol. 77-3 (The Electrochemical
Society, Inc., Princeton,
New Jersey, 1977), p. 84. |
| 4530 | IR Spectroscopy Via Difference-
Frequency Generation | A. S. Pine | In <u>Laser Spectroscopy</u> , edited
by J. L. Hall and J. L. Carlsten
(Springer Series in Optical
Sciences, Vol. 7) (Springer-
Verlag, New York, 1977) |
| 4559 | An Efficient Lensing Element
for X-Rays | N. M. Ceglio*
H. I. Smith | Proc. VIII Intl. Conf. on X-Ray
Optics and Microanalysis,
Boston, 22-26 August 1977 |

* * * * *

UNPUBLISHED REPORTS

Journal Articles

JA No.

- | | | | |
|-------|---|---|------------------------------------|
| 4710 | Micro Fresnel Zone Plates
for Coded Imaging Applications | N. M. Ceglio*
H. I. Smith | Accepted by Rev. Sci. Instrum. |
| 4739A | Measured Compositions and
Laser Emission Wavelengths
of Ga _x In _{1-x} As _y P _{1-y} LPE
Layers Lattice-Matched to
InP Substrates | J. J. Hsieh | Accepted by J. Electron.
Mater. |
| 4754 | Polarized Vibrational Raman
Scattering Lineshape Param-
eters in Liquid CO and Liquid
CO Mixtures | S. R. J. Brueck | Accepted by Chem. Phys.
Lett. |
| 4772 | GaInAsP/InP Double-
Heterostructure Lasers for
Fiber Optic Communications | J. J. Hsieh
C. C. Shen | Accepted by Fiber Integ. Opt. |
| 4775 | Chemisorbed Phases of H ₂ O
on TiO ₂ and SrTiO ₃ | V. E. Henrich
G. Dresselhaus
H. J. Zeiger | Accepted by Solid State
Commun. |

* Author not at Lincoln Laboratory

JA No.

- | | | | |
|------|---|---|-----------------------------------|
| 4780 | Effect of O ₂ Pressure During Deposition on Properties of rf-Sputtered Sn-Doped In ₂ O ₃ Films | J. C. C. Fan
F. J. Bachner
G. H. Foley* | Accepted by Appl. Phys. Lett. |
| 4784 | High-Resistivity Layers in n-InP Produced by Fe Ion Implantation | J. P. Donnelly
C. E. Hurwitz | Accepted by Solid-State Electron. |

Meeting Speeches[†]MS No.

- | | | | |
|-------|---|---|--|
| 4442A | Submicrometer Technology | H. I. Smith | CMSE Colloq., M.I.T.,
14 October 1977 |
| 4447 | Doppler-Limited Infrared Molecular Spectroscopy with a Tunable-Laser Difference-Frequency Converter | A. S. Pine | Fifth Colloq. on High Resolution Molecular Spectroscopy, Tours, France, 19-23 September 1977 |
| 4480A | A New Signal Processing Device, the Integrating Correlator | R. W. Ralston
D. H. Hurlburt
F. J. Leonberger
J. H. Cafarella
E. Stern | } 1977 Ultrasonics Symp.,
Phoenix, Arizona,
26-28 October 1977 |
| 4545 | Filter with Bandwidth Continuously Variable from 5 to 100 MHz | J. Melngailis
R. C. Williamson
R. H. Domnitz* | |
| 4547 | Acoustoelectrically Scanned Gap-Coupled Si-Diode Array/LiNbO ₃ Imaging Devices | F. J. Leonberger
J. H. Cafarella
R. W. Ralston
E. Stern
A. L. McWhorter | |
| 4548 | 310-MHz SAW Resonator with Q at the Material Limit | R. C. M. Li | |
| 4560 | Case Studies of Successful Surface-Acoustic-Wave Devices | R. C. Williamson | |
| 4501 | X-Ray Replication of Sub-micrometer Linewidth Patterns | H. I. Smith
D. C. Flanders | 35th Annual Mtg. EMSA, Boston, 22-26 August 1977 |
| 4540 | Resonant Infrared Four-Wave Mixing in Cryogenic Liquids | S. R. J. Brueck
H. Kildal | 1977 Fall Mtg. of Optical Society of America, Toronto, Ontario, Canada, 10-14 October 1977 |

* Author not at Lincoln Laboratory.

† Titles of Meeting Speeches are listed for information only. No copies are available for distribution.

MS No.

4542, A	Recent Advances in Laser Devices	A. Mooradian	9th Intl. Conf. on Solid Devices, Tokyo, Japan, 30-31 August 1977; U.S.-Japan Symp. on Laser Spectroscopy, Hakone, Japan, 4-8 September 1977
4543	Chemisorbed Phases of O ₂ on TiO ₂ and SrTiO ₃	V. E. Henrich G. Dresselhaus H. J. Zeiger	24th Natl. Vacuum Symp., Boston, 8-11 November 1977
4544	Surface Photovoltage Experiments on SrTiO ₃ Electrodes	J. G. Mavroides D. F. Kolesar	
4546	Advances in Narrow-Gap Semiconductor Electrooptical Devices	I. Melngailis	III Intl. Conf. on the Physics of Narrow-Gap Semiconductors, Warsaw, Poland, 12-15 September 1977
4555	Fabrication and Alignment of Submicrometer Structures	H. I. Smith	Colloquium, Sperry Rand Research Center, Sudbury, Massachusetts, 15 August 1977
4561	High-Efficiency GaAs Shallow-Homojunction Solar Cells	J. C. C. Fan C. O. Bozler	1977 Fall Mtg. of Electrochemical Society, Atlanta, Georgia, 9-14 October 1977
4571	Submicrometer Pattern Replication and Alignment Using X-Ray Lithography	D. C. Flanders	Semicon East '77, Boston, 19 September 1977

ORGANIZATION

SOLID STATE DIVISION

A. L. McWhorter, *Head*
 I. Melngailis, *Associate Head*
 C. R. Grant, *Assistant*
 P. E. Tannenwald

QUANTUM ELECTRONICS

A. Mooradian, *Leader*
 P. L. Kelley, *Associate Leader*

Barch, W. E.	Fleming, M. W.*
Brueck, S. R. J.	Hancock, R. C.
Burke, J. W.	Kildal, H.
Chinn, S. R.	Menyuk, N.
DeFeo, W. E.	Moulton, P. F.
Deutsch, T. F.	Osgood, R. M.
Duffy, P. E.	Parker, C. D.
Ehrlich, D. J.	Pine, A. S.
Fetterman, H. R.	

APPLIED PHYSICS

A. G. Foyt, *Leader*
 T. C. Harman, *Assistant Leader*
 C. E. Hurwitz, *Assistant Leader*

Armiento, C. A.*	Leonberger, F. J.
Belanger, L. J.	Lind, T. A.
Calawa, A. R.	McBride, W. F.
Carter, F. B.	Paladino, A. E.
DeMeo, N. L., Jr.	Plonko, M. C.
Diadiuk, V.*	Shen, C. C.
Donnelly, J. P.	Spears, D. L.
Ferrante, G. A.	Tsang, D. Z.*
Glasser, L. A.*	Walpole, J. N.
Groves, S. H.	

ELECTRONIC MATERIALS

A. J. Strauss, *Leader*
 H. J. Zeiger, *Associate Leader*

Anderson, C. H., Jr.	Kafalas, J. A.
Bayard, M. L.	Kolesar, D. F.
Button, M. J.	Krohn, L., Jr.
Chapman, R. L.	LaFleur, W. J.
Davis, F. M.	Mastromattei, E. L.
Delaney, E. J.	Mavroides, J. G.
Fahey, R. E.	Mroczkowski, I. H.
Fan, J. C. C.	Owens, E. B.
Feldman, B.	Palm, B. J.
Finn, M. C.	Pantano, J. V.
Gay, R. R.*	Reed, T. G.
Henrich, V. E.	Smith, D. D.
Hong, H. Y-P.	Tchernev, D. I.
Hsieh, J. J.	Tracy, D. M.
Iseler, G. W.	Vohl, P.

SURFACE WAVE TECHNOLOGY

E. Stern, *Leader*
 R. C. Williamson, *Associate Leader*

Baker, R. P.	Kernan, W. C.
Brogan, W. T.	Li, R. C. M.
Cafarella, J. H.	Melngailis, J.
Dolat, V. S.	Ralston, R. W.
Efremow, N., Jr.	Reible, S. A.
Holtham, J. H.	Schulz, M. B.
Hurlburt, D. H.	Slattery, R. L.

MICROELECTRONICS

W. T. Lindley, *Leader*
 F. J. Bachner, *Associate Leader*
 H. I. Smith, *Assistant Leader*

Beatrice, P. A.	Gray, R. V.
Bozler, C. O.	Hansell, G. L.*
Burke, B. E.	Lincoln, G. A., Jr.
Chiang, A. M.	McGonagle, W. H.
Clifton, B. J.	Mountain, R. W.
Clough, T. F.	Murphy, R. A.
Daniels, P. J.	Pichler, H. H.
DeGraff, P. D.	Shaver, D. C.*
Durant, G. L.	Silversmith, D. J.
Felton, B. J.	Smythe, D. L., Jr.
Flanders, D. C.	Wilde, R. E.
Grant, L. L.	

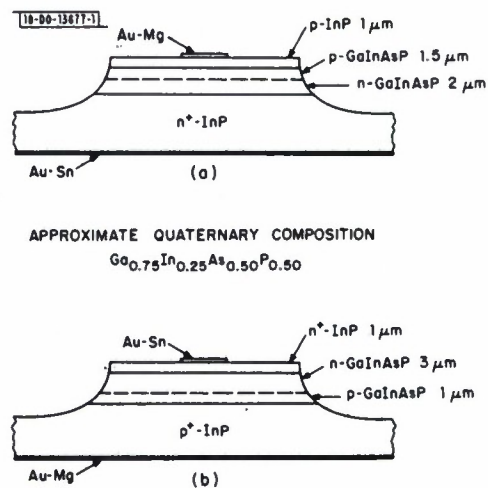
* Research assistant

I. SOLID STATE DEVICE RESEARCH

A. GaInAsP/InP AVALANCHE PHOTODIODES

Avalanche multiplication of a photosignal has been observed for the first time in diodes of the quaternary alloy GaInAsP. The diodes, which were fabricated from quaternary layers lattice-matched to InP substrates, had a long-wavelength cutoff of $1.25\ \mu\text{m}$, although diodes having a response cutoff out to $1.6\ \mu\text{m}$ are possible in this quaternary system with compositions still lattice-matched to InP. Avalanche diodes in the GaInAsP material system are expected to have important applications in the fields of fiber optics communications and integrated optical circuits. Recently, avalanche multiplication at $1.2\ \mu\text{m}$ in the ternary alloy GaInAs, lattice-matched to an InP substrate, as well as normal photodiode operation in GaInAsP have been reported in the literature.^{1,2}

Fig. I-1. Schematic diagram of (a) normal and (b) inverted mesa GaInAsP/InP photodiode structures.



Multiplication has been observed in the two similar etched mesa diode structures shown schematically in Fig. I-1(a-b). In both cases, the quaternary and top InP layers were grown by liquid-phase epitaxy (LPE) on InP substrates, with the nominal composition of the quaternary layers in the two structures being $\text{Ga}_{0.75}\text{In}_{0.25}\text{As}_{0.50}\text{P}_{0.50}$. In the structure shown in Fig. I-1(a), the quaternary and capping InP layers were initially undoped ($n \approx 1$ to $3 \times 10^{16}\ \text{cm}^{-3}$), and the p-n junction was formed by diffusing Zn (an acceptor) through the top InP layer into the GaInAsP. C-V measurements indicated that the junction was graded over a range of $1.9\ \mu\text{m}$, with the net donor concentration increasing from $8 \times 10^{15}\ \text{cm}^{-3}$ at the zero-bias depletion layer edge to $2 \times 10^{16}\ \text{cm}^{-3}$, a value characteristic of the as-grown layer. This shape of graded layer presumably corresponds to that of the Zn diffusion front.

Mesas of $150\text{-}\mu\text{m}$ diameter were etched using 1-percent Br in methanol or a 1:6:1:1 solution of $\text{HCl}:\text{HNO}_3:\text{HAc}:\text{HClO}_4$. Contacts of evaporated Au-Mg (p-type) and plated Au-Sn (n-type) were alloyed at 400°C . Breakdown voltages of the diodes were in the 50- to 60-V range. The spectral

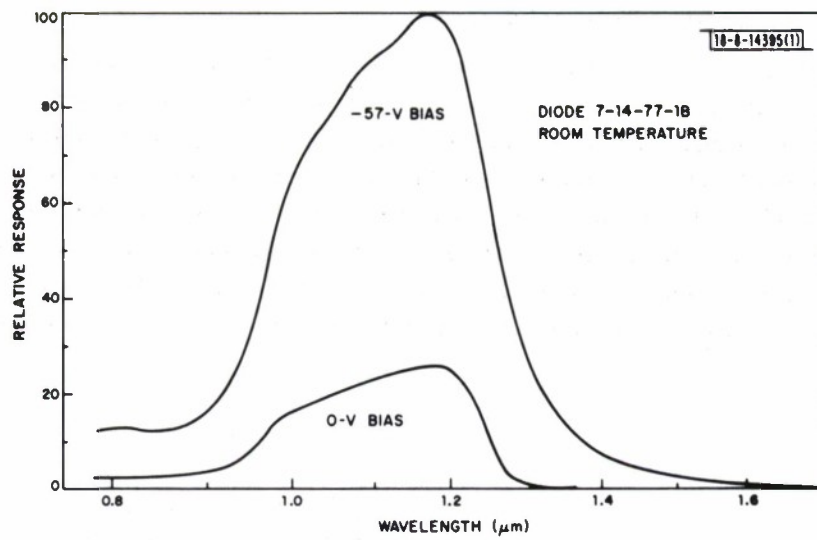


Fig. I-2. Spectral response of GaInAsP/InP photodiode at zero bias and with sufficient reverse bias to cause avalanche gain of about 4.

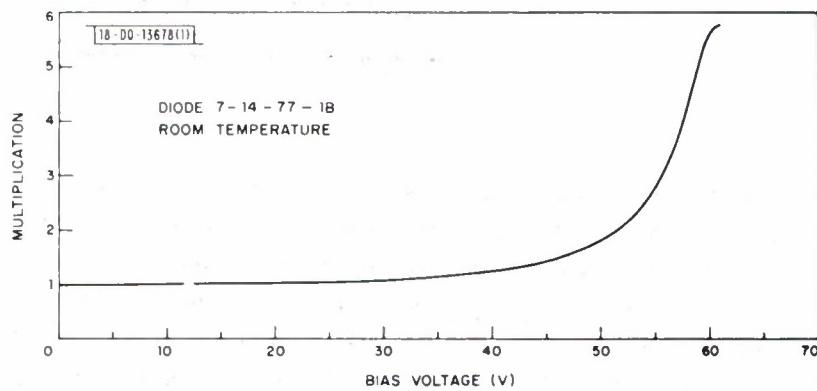


Fig. I-3. Multiplication vs applied bias for same diode as in Fig. I-2. Excitation wavelength was 1.17 μm .

response of one of the devices with and without bias is shown in Fig. I-2. Illumination was from the direction of the top contact, although the transparent InP substrate and top layer will permit illumination from either direction. This feature will be highly useful in future experiments to measure electron and hole ionization rates. The observed signal increase with bias corresponds to an avalanche gain of about 4. The shift of the response cutoff to longer wavelengths at the higher bias is presumably due to the Franz-Keldysh effect, as has been observed in GaAs avalanche diodes.³ Figure I-3 shows the multiplication vs applied voltage for the same diode with 1.17- μm excitation.

The uniformity of response of the devices was also examined with a raster-scanned focused spot from a 1.15- μm GaInAsP/InP laser. The response was quite uniform up to biases yielding a gain of 4 or 5. For higher reverse voltages, there was a rapid increase in multiplied signal at the edge of the mesa, indicating the onset of edge breakdown. This behavior is to be expected from the normal mesa geometry because of the higher field at the junction periphery due to field crowding.

To reduce the gain limitation due to edge breakdown, the inverted mesa structure shown in Fig. I-1(b) was fabricated and tested. Again, the GaInAsP layer was not intentionally doped, and the p-n junction was formed by diffusion of Zn, this time by outdiffusion from the heavily Zn-doped InP substrate. Contacts were applied and mesas etched as before. Again, the C-V measurements indicated a graded junction with characteristics similar to those described above. However, these diodes had somewhat higher breakdown voltages (65 to 70 V), showed no evidence of edge multiplication, and gave somewhat higher values of gain (as high as 12). A typical I-V characteristic for one of the devices is shown in Fig. I-4. Raster scans of the diode response to a 1.15- μm laser for conditions of no gain and for a gain of about 8 are shown in Fig. I-5(a-b). For higher biases, the multiplication appears to be limited by microplasma breakdown and/or by excess leakage current, possibly at the unpassivated surface.

Initial measurements of the low-bias quantum efficiency and speed of response of the diodes were also made. The quantum efficiency at 1.15 μm was approximately 45 percent. When biased to yield a gain of about 8, the risetime of the avalanche diode response to a pulse from a GaInAsP/InP laser was less than 200 psec. At present, we have not determined whether the observed risetime is characteristic of the laser or detector.

Present experiments are directed toward increasing the attainable multiplication by lowering the GaInAsP carrier concentration, developing better guard-ring techniques, eliminating surface leakage currents, and reducing the substrate and layer dislocation densities to reduce microplasmas. Measurements of the electron and hole ionization rates as well as more refined speed and quantum efficiency measurements will also be made.

C. E. Hurwitz
J. J. Hsieh
R. L. Payer

B. EPITAXIAL HOMOSTRUCTURE $\text{Pb}_{1-x}\text{Sn}_x\text{Te}$ DIODE LASERS WITH CW OPERATION UP TO 100 K

We report CW operation of epitaxially grown $\text{Pb}_{1-x}\text{Sn}_x\text{Te}$ homojunction diode lasers for heat-sink temperatures up to 100 K. This temperature is comparable to the maximum temperatures reported (80 to 120 K) for CW operation of single or double heterostructures in any of the lead-tin chalcogenides (lead salts).

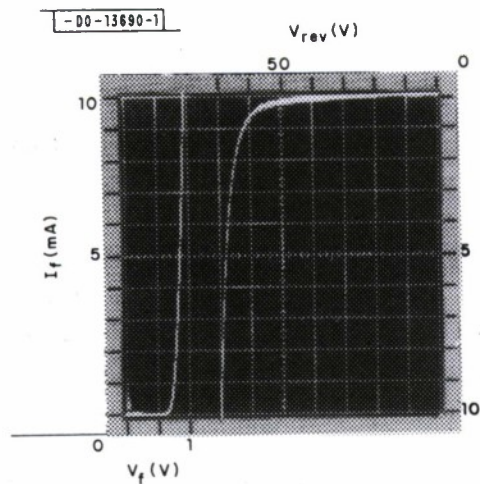


Fig.I-4. Forward and reverse I-V characteristics of typical inverted mesa device.

DIODE 9-8-77-4B-G6
 AREA = $1.8 \times 10^{-4} \text{ cm}^2$

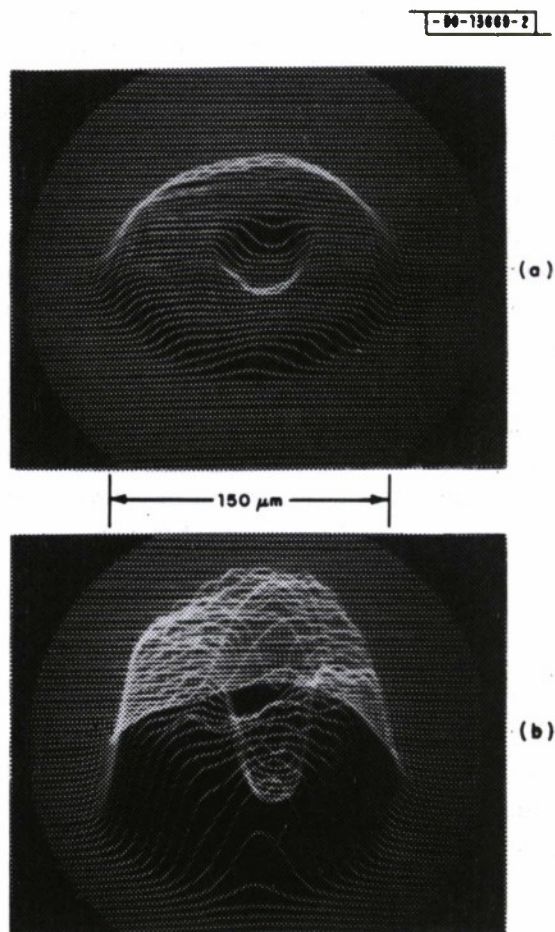


Fig.I-5. Raster scans at 1.15- μm excitation of 150- μm -diam inverted mesa avalanche diode. Scan (a) is at 24-V bias and little or no gain ($M \approx 1$). Scan (b) is at 71.8-V reverse voltage and corresponds to multiplication (M) of about 8.

In the lead salts, because of the small effective masses of both electrons and holes and because of the small energy gaps, strong optical and carrier confinement can be achieved, in principle, with properly controlled carrier-concentration profiles.⁴ As demonstrated here, CW operation at least to temperatures moderately above that of liquid nitrogen can be achieved without heterostructures through the use of epitaxial techniques and foreign impurity dopants to obtain the control of concentration profile required. Hence, epitaxial homostructures can have the advantages of heterostructures while eliminating the problems associated with mismatches in lattice constants and thermal expansion coefficients, factors suspected of contributing to lower quantum efficiency and device degradation.

Devices were grown by both molecular-beam epitaxy (MBE) and liquid-phase epitaxy (LPE) using techniques previously reported^{5,6} to obtain n^+-n-p^+ doping profiles. Two compositions, $x = 0$ and $x = 0.22$, were grown by MBE. Both were grown in a stripe geometry using MgF_2 growth masks with 10- μm -wide stripes. The growth masks, however, cracked during growth so that growth occurred outside the stripes (i.e., in the cracks). Consequently, the junction area was not accurately determined. A lower limit of $3.2 \times 10^{-5} \text{ cm}^2$ is the area of the stripes alone. Bi-doped active regions ($n \approx 5 \times 10^{17} \text{ cm}^{-3}$) 1.5 μm thick followed by Bi-doped capping layers ($n^+ \approx 5 \times 10^{18} \text{ cm}^{-3}$) 0.75 μm thick were grown on Tl-doped substrates ($p^+ \approx 10^{19} \text{ cm}^{-3}$).

The LPE devices were grown for $x = 0$ only, using growth masks of 50- μm -wide stripes on p^+ Tl-doped substrates. The active n-region was undoped and probably had a carrier concentration of $n \approx 1 \times 10^{17} \text{ cm}^{-3}$ due to stoichiometric defects characteristic of growth from a Pb-rich solution at 500°C. Indium rather than Bi doping was used for the n^+ capping layer because of its higher doping efficiency in the Pb-rich solution growth. The carrier concentration was estimated to be $n^+ \approx 4 \times 10^{18} \text{ cm}^{-3}$.

In Fig. I-6, CW threshold current vs heat-sink temperature for the homostructure devices are compared with earlier data for double-heterostructure devices. Threshold current densities cannot be compared for the MBE devices because of the uncertainty in junction area mentioned above. Although slightly higher temperature of operation was achieved with the DH lasers (~115 K), the MBE homostructures operated to ~100 K and the LPE homostructures operated to ~80 K. Moreover, relatively large output powers were observed for the $x = 0$ devices, the maximum observed being 4.5-mW single-ended output from an LPE homostructure at ~15 K. At slightly lower power levels, the output tended to be in a single mode, as shown in Fig. I-7 for an MBE homostructure PbTe laser with 2.4-mW output at 15 K and 0.64-mW output at 102 K. The $Pb_{0.78}Sn_{0.22}Te$ homostructures showed maximum output powers of only ~0.4 mW at 15 K and ~0.12 mW at 80 K, which nevertheless are somewhat better powers than typically observed in MBE DH lasers.⁵

The improvement in output power observed in the homostructures is encouraging. Device degradation has not been studied carefully as yet, since a number of factors appear to be involved including packaging techniques. In any event, the use of homostructures may be an attractive alternative to the use of ternary alloy substrates such as $PbTe_{1-y}Se_y$ (Ref. 7) to achieve lattice matching in the lead salts.

J. N. Walpole
S. H. Groves
T. C. Harman

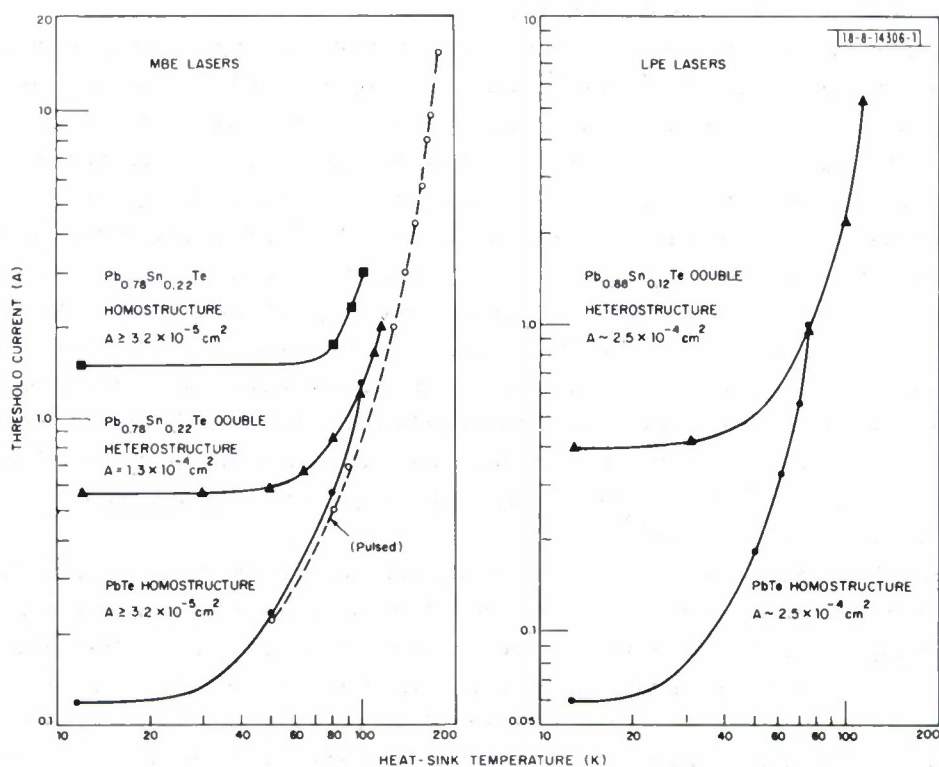


Fig.1-6. CW threshold current vs heat-sink temperature for various homostructure and double-heterostructure $\text{Pb}_{1-x}\text{Sn}_x\text{Te}$ lasers grown by MBE and by LPE.

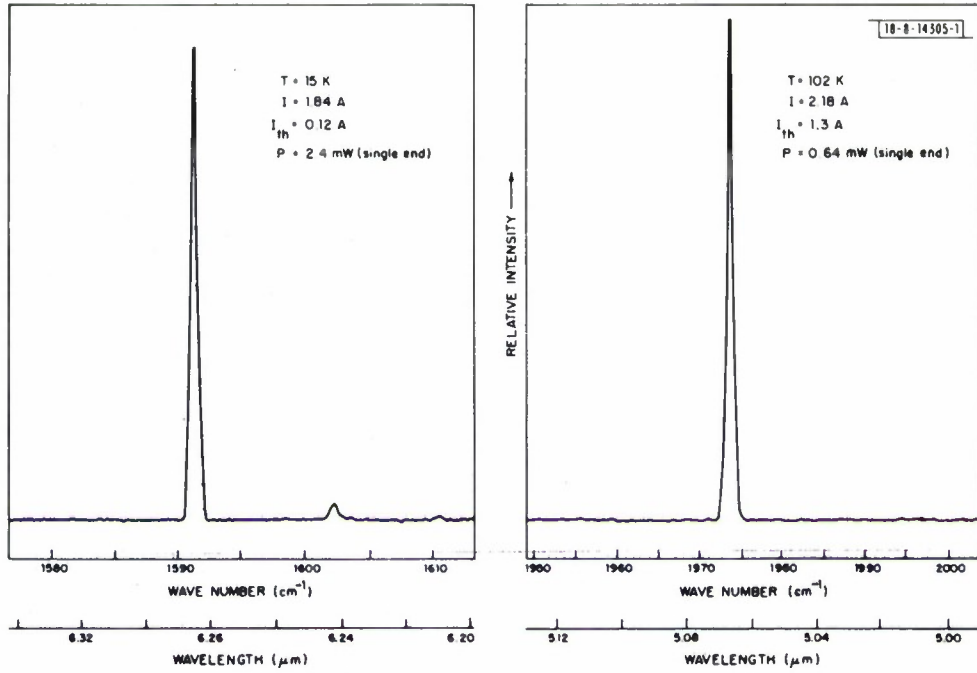


Fig. I-7. CW spectra of an MBE PbTe homostructure laser at 15- and 102-K heat-sink temperatures, showing nearly single-mode behavior at relatively large output power levels.

C. HIGH-RESISTIVITY LAYERS IN n-InP PRODUCED BY Fe-ION IMPLANTATION

The ability to selectively form high-resistivity layers in GaAs and related Ga-based III-V compounds by proton bombardment⁸⁻¹⁷ or oxygen ion implantation¹⁸ has been used to advantage in the fabrication of a wide variety of microwave and optoelectronic devices. (For a summary of applications see, for example, Refs. 19 or 20.) More recently, this technique has been used successfully with InP to fabricate stripe-geometry InP/InGaAsP lasers.^{21,22} However, in InP, we observed that, although proton bombardment can result in increases of the resistivity of p-type material to greater than $10^8 \Omega\text{-cm}$, the maximum observed resistivity of proton-bombarded n-type InP was approximately $10^3 \Omega\text{-cm}$ (Refs. 23 and 24). In an effort to obtain higher resistivities in n-type material, we investigated the implantation of Fe, an impurity which is known to result in high-resistivity InP when used as a dopant during growth of bulk crystals.²⁵ We found that the implantation of Fe^+ followed by a suitable anneal can increase the resistivity of n-type InP to at least $10^7 \Omega\text{-cm}$. In this section, we discuss the implantation and anneal procedures and present our initial experimental results.

The n-InP samples used in these experiments were cut from (111)-oriented crystals grown by the liquid-encapsulation Czochralski technique and had carrier concentrations of $(4 \text{ to } 7) \times 10^{16} \text{ cm}^{-3}$ or $\approx 1 \times 10^{18} \text{ cm}^{-3}$. After polishing, the samples were etched in a 1:1:6:1 solution of $\text{HAc}:\text{HClO}_4:\text{HNO}_3:\text{HCl}$ (Ref. 26). Implants of Fe^+ were performed at both room temperature and 200°C with the samples tilted in reference to the ion beam to minimize channeling. A multiple-energy implantation schedule was used on all samples in an attempt to create a layer with a uniform Fe concentration. The range and range-straggling statistics were obtained using

a computer program developed by Johnson and Gibbons²⁷ and based on LSS theory.²⁸ The multiple-dose schedule selected was N at 400 keV, 0.36 N at 190 keV, 0.18 N at 90 keV, and 0.1 N at 40 keV (where N is in units of cm^{-2}).

Following implantation, each sample was encapsulated with 2500 Å of pyrolytic phosphosilicate glass (PSG) deposited at 250°C. Details of this procedure can be found in Ref. 29. Samples were then annealed in flowing nitrogen. In preliminary experiments, the anneal temperature was varied from 650° to 750°C and the anneal time from less than 1 min. (pulse heating) to 15 min. Although good results were obtained over a rather broad range of anneal temperatures and times, an anneal at 725°C for 15 min. generally resulted in layers of the highest resistivity and was used almost exclusively in subsequent experiments. As discussed below, however, the anneal schedule does influence the amount of diffusion of the implanted Fe and may have to be modified for specific applications.

After annealing, holes were opened in the PSG, through which 5- to 15-mil-diam gold contacts were plated on the Fe-implanted layers. Illumination from a microscope lamp was used during plating to achieve sufficient electrical conductivity in the insulating layer. A large-area gold back contact, with a measured contact resistance of a few ohms, was plated on the n-type substrate. To evaluate the effects of the Fe-ion implantations, the current-voltage and capacitance-voltage characteristics as well as the equivalent zero-bias parallel resistance and capacitance of the Au/Fe-implanted InP/n-substrate structures were measured.

For material with an initial carrier concentration in the range of $(4 \text{ to } 7) \times 10^{16} \text{ cm}^{-3}$, multi-energy Fe implants with doses corresponding to $N = 5 \times 10^{12}$ to $1 \times 10^{14} \text{ cm}^{-2}$ were investigated. Maximum zero-bias resistances ($RA > 6 \times 10^3 \Omega\text{-cm}^2$) were obtained for $N = (2 \text{ to } 6) \times 10^{13} \text{ cm}^{-2}$. For material with an initial concentration of about 10^{18} cm^{-3} , a dose of $N \approx 4 \times 10^{14} \text{ cm}^{-2}$ gave the highest resistance. However, the value of this resistance was typically 5 to 10 times lower than that obtained in the more lightly doped material. Figure I-8 shows the current-voltage characteristics of a 5-mil-diam Au contact on an InP sample with an initial concentration of $6 \times 10^{16} \text{ cm}^{-3}$, which was implanted with a multi-energy Fe schedule with $N = 4 \times 10^{13} \text{ cm}^{-2}$ and annealed at 725°C for 15 min. The difference in breakdown voltage between the forward direction (top contact positive) and the reverse direction is at least partially due to the increase of the depletion-layer thickness in the n-type substrate with increasing

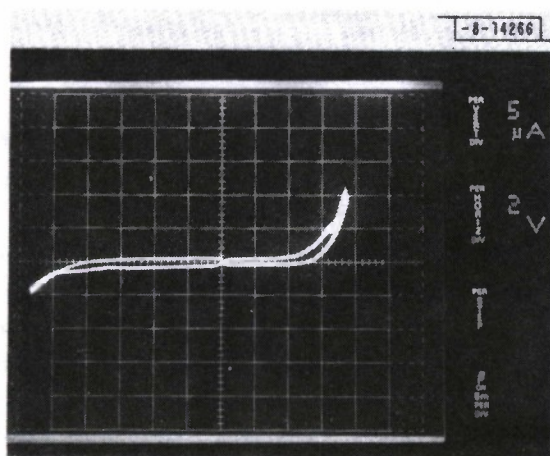


Fig. I-8. Current-voltage characteristics of 5-mil-diam gold contact on $N = 6 \times 10^{16} \text{ cm}^{-3}$ InP after room-temperature multi-energy Fe^+ implantation with $N = 4 \times 10^{13} \text{ cm}^{-2}$ (see text) followed by 725°C, 15-min. anneal.

reverse bias. The zero-bias resistance is greater than 50 M Ω and the zero-bias capacitance is 1.87 pF, from which one deduces that the high-resistivity layer is about 0.8 μm thick and has an average resistivity of $6 \times 10^7 \Omega\text{-cm}$.

The 0.8- μm depth of the implanted Fe^+ ions is much greater than expected from LSS theory²⁸ for the implant schedule used. Furthermore, samples implanted with the same schedule but annealed at lower temperatures exhibit higher capacitances and presumably have thinner high-resistivity layers. For example, 5-mil-diam Au contacts on a sample annealed at 650°C had capacitances of 2.70 pF, while those on a sample annealed at 700°C had capacitances of 2.37 pF. In the range of 1 to 15 min., increasing anneal times also resulted in decreased values of capacitance. These results indicate that considerable diffusion of the implanted Fe must be taking place during the post-implantation anneal. Samples implanted at 200°C also exhibited higher capacitances than similar samples implanted at room temperature, indicating that the Fe diffusion can be reduced by implanting into heated substrates.

Depth profiles of effective carrier concentrations in the layers were obtained from capacitance-voltage measurements. The effective carrier concentration, n_{eff} , was calculated using the well-known relations

$$n_{\text{eff}}(x) = \frac{C^3}{q\epsilon A^2 \left(-\frac{dC}{dV}\right)} \quad \text{and} \quad x = \frac{\epsilon A}{C}$$

where $n_{\text{eff}}(x)$ is the effective carrier concentration at depth x , C is the capacitance, A is the area of the diode, V is the applied voltage (assumed positive in the reverse direction), q is the electronic charge, and ϵ is the static dielectric constant for InP. Figure I-9 shows the results of measurements made at 500 kHz on two samples, one implanted at room temperature and the other at 200°C with the same multi-energy Fe-implant schedule ($N = 4 \times 10^{13} \text{ cm}^{-2}$). Both samples were annealed at 725°C for 15 min. Also shown is the as-implanted Fe profile expected from LSS theory.²⁸ In agreement with the zero-bias capacitance measurements, the low-carrier-concentration region (high-resistivity region) of the room-temperature implant is $\approx 0.8 \mu\text{m}$ thick. On the other hand, the high-resistivity region in the sample implanted at 200°C is only $\approx 0.55 \mu\text{m}$, which is closer to the calculated profile, again indicating that diffusion during anneal is less for the hot implants.

Both samples shown in Fig. I-9 appear to have an anomalous carrier-concentration peak at the edge of the high-resistivity region, similar to those which have been observed in proton-bombarded GaAs (see Refs. 9 and 12). We do not believe that these peaks are real "donor peaks," and we suggest the following alternative explanation. Figure I-10 is a representation of the band diagram of our structure, assuming that the Fe acts as a simple deep acceptor near the middle of the gap and that the Fermi level at the surface is pinned about one-third of the way down from the conduction band edge. For the implanted layer to be high resistivity, the Fermi level must be near the center of the gap which, in turn, requires that the implanted Fe concentration must be greater than about twice the donor concentration. This requirement also makes the "effective Debye length" in the high-resistivity implanted region short enough so the space-charge regions at the substrate interface and at the Au contact extend only a short distance into the implanted layer. Due to band-bending near the interface, the Fe levels in this region will drop below the Fermi level, and in equilibrium the excess Fe levels will be filled. Although a detailed analysis of this model has not yet been completed, we believe that the charging and discharging

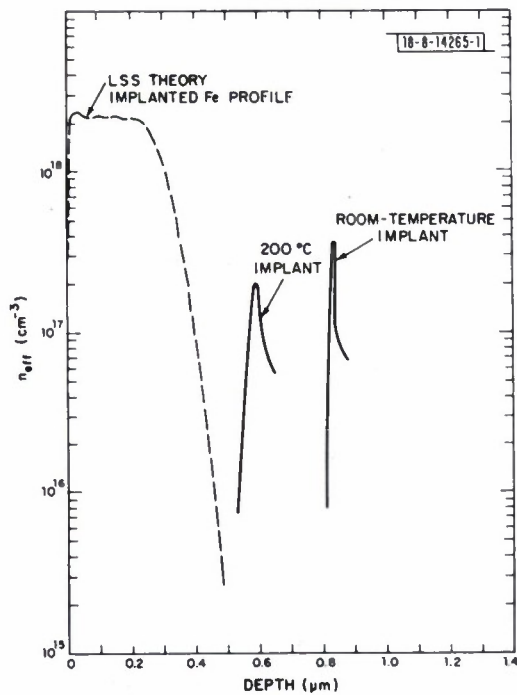
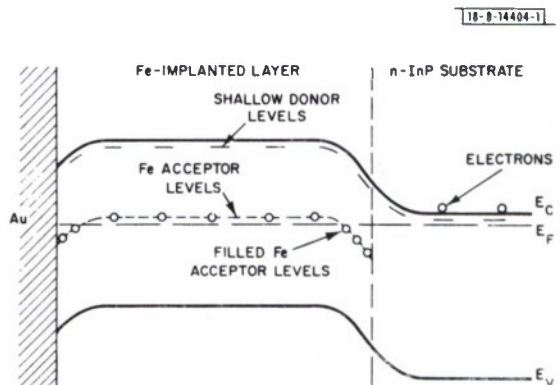


Fig.I-9. Effective carrier concentration vs depth obtained from capacitance-voltage measurements for two InP ($N = 6 \times 10^{16} \text{ cm}^{-3}$) samples after a multi-energy Fe^+ implant and a 725°C , 15-min. anneal. One sample was implanted at room temperature, and the other at 200°C .

Fig.I-10. Representative band diagram of Fe-implanted n-type InP indicating filling of excess Fe levels at interface.



of the Fe levels with a change in applied bias[†] can result in what appears to be a peak in the carrier concentration. Emission from deep levels has also been proposed¹² to explain similar results in proton-bombarded GaAs.

In addition to the implants into bare n-InP samples, we have made some implants through 500 Å of PSG or an anodic oxide. Although the results were not as reproducible as those for samples implanted bare, high-resistivity layers with $\rho \geq 10^7 \Omega\text{-cm}$ were obtained. The depth of the high-resistivity region was approximately 0.66 μm for a room-temperature implant ($N = 4 \times 10^{13} \text{ cm}^{-2}$) made through a 500-Å layer of PSG.

J. P. Donnelly
C. E. Hurwitz

D. POST-TO-PAD INDIUM-TO-INDIUM LEAD BONDING

A technique for bonding to small bonding pads on soft semiconductor materials with high yield and good reliability has been developed. In conventional lead bonding, a wire or ribbon is first fused to a bonding pad on the chip and then draped over a bonding post, bonded, and cut. These pad-to-post techniques require bending the ribbon or wire after the pad bond is made, and consequently puts stress on this bond. The exact amount of stress is difficult to control, as it depends upon the stiffness of the wire or ribbon and any mechanical motion of the wire or ribbon needed to complete the post bond. This stress presents a major problem when the size of the bonding pad is small and when only low temperatures and pressures are allowed in making the pad bond, e.g., in the case of the bonding pads for wide-bandwidth HgCdTe photodiodes.³⁰ These problems have been solved by a post-to-pad bonding process, which utilizes In-to-In bonds at both the post and pad positions and soft gold lead ribbon to minimize bonding temperature, pressure, and stress in the lead.

The post-to-pad In-to-In bonding technique is shown schematically in Fig. I-11. The first step is the vacuum deposition of a 1- to 2- μm -thick layer of In on one surface of 7- \times 38- μm soft-gold ribbon. One end of a strip of ribbon is placed in a microalligator clip and the ribbon cut off to a length of about 5 mm. The ribbon is positioned with the In side down over an In-coated (about 5- μm -thick) bonding post on the chip package. A bonding stylus with a 38- μm -diam tip is brought down, tacking the ribbon to the post. However, before the stylus is released, the clip is pulled away, breaking off the ribbon. The ribbon is secured to the In-coated post by tapping the ribbon with the stylus. By pressing the stylus into the ribbon and moving the stylus sideways, the ribbon can be repositioned to the exact location desired. By pressing on the ribbon near the edge of the bonding post, the ribbon can be bent downward so that the end of the ribbon is touching the bonding pad. A 5° to 10° bend appears to be optimum for bonding. In the final bonding step, the 160°C heated stylus is brought down slowly with a limiting force of 7 g, making contact for about 1 sec, and released.

A 0.5-mm-diam, 12-element array of HgCdTe photodiodes bonded in this fashion is shown in Fig. I-12. To date, over 200 bonds have been made by this process with a yield of about 95 percent and a contact resistance much less than 1 ohm. The few bad leads were simply removed and replaced with a new ribbon, as the titanium (500 Å) plus gold (3000 Å) plus

[†] For the band structure shown in Fig. I-10, this is essentially a single-carrier problem and is similar to single injection with traps. For example, see M. A. Lampert and R. B. Schilling, in Semiconductors and Semimetals, Vol. 6, R. K. Willardson and A. C. Beer, Eds. (Academic Press, New York, 1970), p. 1.

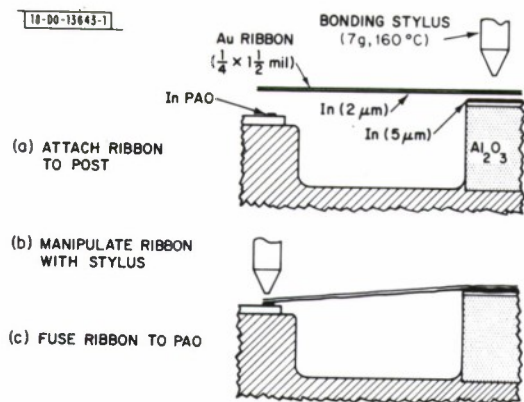
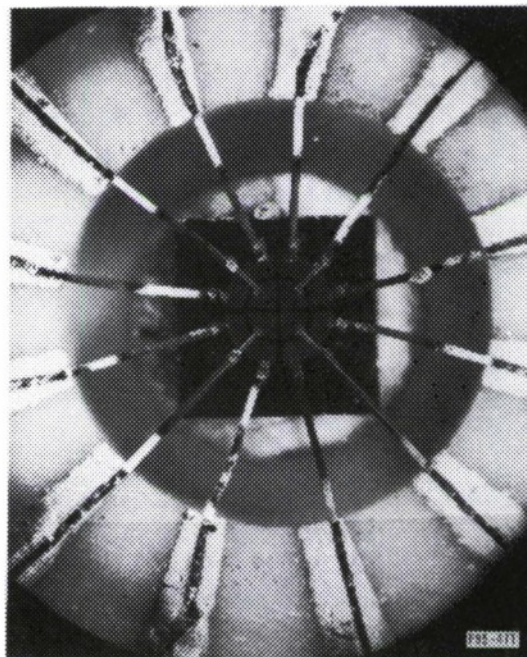


Fig.I-11. Schematic diagrams depicting two steps in post-to-pad In-to-In lead-bonding technique.

Fig.I-12. A 0.5-mm-diam, 12-element HgCdTe photodiode array bonded in a chip package.



indium ($10,000 \text{ \AA}$) bonding pads are not degraded during the bonding process. Bonds have also been readily made to Au bonding pads not coated with In, and, in fact, directly to the n-type region of an n/p HgCdTe diode without apparent degradation of its I-V characteristics. Although the full range of stylus temperatures and pressures over which such bonding can be done has not been explored, the process does not seem to be particularly sensitive to the parameters used (160°C and 7 g). This technique does provide a relatively simple means of attaching reliable leads to small bonding pads on soft semiconductor materials without apparent damage, and has allowed arrays of gigahertz-bandwidth HgCdTe heterodyne receivers to be fabricated.

D. L. Spears
C. D. Hoyt
N. L. DeMeo

REFERENCES

1. T. P. Pearsall and R. W. Hopson, Jr., *J. Electron. Mater.* 7, 133 (1978) (to be published).
2. H. H. Wieder, A. R. Clawson, and G. E. McWilliams, *Appl. Phys. Lett.* 31, 468 (1977).
3. G. E. Stillman, C. M. Wolfe, J. A. Rossi, and J. P. Donnelly, *Appl. Phys. Lett.* 25, 671 (1974), DDC AD-A006705/8.
4. P. M. Asbeck, Ph.D. Thesis, M.I.T., 1975 (unpublished).
5. J. N. Walpole, A. R. Calawa, T. C. Harman, and S. H. Groves, *Appl. Phys. Lett.* 28, 552 (1976), DDC AD-A027012/4.
6. S. H. Groves, K. W. Nill, and A. J. Strauss, *Appl. Phys. Lett.* 25, 331 (1974), DDC AD-A002773/0.
7. Solid State Research Report, Lincoln Laboratory, M.I.T. (1974:4), p. 13, DDC AD-A004763/9.
8. K. Wohleben and W. Beck, *Z. Naturforsch. A* 21A, 1057 (1966).
9. A. G. Foyt, W. T. Lindley, C. M. Wolfe, and J. P. Donnelly, *Solid-State Electron.* 12, 209 (1969), DDC AD-694145.
10. J. C. Dymant, J. C. North, and L. A. D'Asaro, *J. Appl. Phys.* 44, 207 (1973).
11. B. R. Pruniaux, J. C. North, and G. C. Miller, in Proceedings of the International Conference on Ion Implantation in Semiconductors, 1971 (Springer-Verlag, Berlin, 1971), p. 212.
12. H. Haradu and M. Fujimoto, in Proceedings of the International Conference on Ion Implantation in Semiconductors, 1974 (Plenum, New York, 1975), p. 73.
13. J. P. Donnelly and F. J. Leonberger, *Solid-State Electron.* 20, 183 (1977), DDC AD-A040521/7.
14. J. D. Speight, P. O'Sullivan, P. A. Leigh, N. McIntyre, K. Cooper, and J. O'Hara, in Gallium Arsenide and Related Compounds (Edinburgh), 1976 (The Institute of Physics, London, 1977), Conf. Ser. 33a, p. 275.
15. J. C. Dymant, L. A. D'Asaro, J. C. North, B. I. Miller, and J. E. Ripper, *Proc. IEEE* 60, 726 (1972).
16. P. N. Favennec and D. Diguët, *Appl. Phys. Lett.* 23, 546 (1973).
17. P. M. Spitzer and J. C. North, *J. Appl. Phys.* 44, 214 (1973).
18. P. N. Favennec, *J. Appl. Phys.* 47, 2532 (1976).

19. P. L. F. Hemment, in Applications of Ion Beams to Materials, 1975 (The Institute of Physics, London, 1976), Conf. Ser. 28, p. 44.
20. J. P. Donnelly, Chapter 4 in Gallium Arsenide and Related Compounds (St. Louis) 1976, edited by L. F. Eastman (The Institute of Physics, London, 1977), Conf. Ser. 33b, p. 166.
21. J. J. Hsieh, J. A. Rossi, and J. P. Donnelly, Appl. Phys. Lett. 28, 709 (1976), DDC AD-A028550/2.
22. J. A. Rossi, J. J. Hsieh, and J. P. Donnelly, Chapter 6 in Gallium Arsenide and Related Compounds (St. Louis) 1976, edited by L. F. Eastman (The Institute of Physics, London, 1977), Conf. Ser. 33b, p. 303.
23. J. P. Donnelly and C. E. Hurwitz, Solid-State Electron. 20, 727 (1977).
24. Solid State Research Report, Lincoln Laboratory, M.I.T. (1977-2), p. 6, DDC AD-A044795.
25. O. Mizuno and H. Watanabe, Electron. Lett. 11, 118 (1975).
26. R. Becker, Solid-State Electron. 16, 1241 (1973).
27. W. Johnson and J. F. Gibbons, Projected Range Statistics in Semiconductors (Stanford University Bookstore, Stanford, California, 1970).
28. J. Lindhard, M. Scharff, and H. Schiott, K. Dan. Vidensk. Selsk. Mat.-Fys. Medd. 33, 1 (1963).
29. J. P. Donnelly and C. E. Hurwitz, Appl. Phys. Lett. 31, 418 (1977).
30. D. L. Spears, Infrared Phys. 17, 5 (1977).

II. QUANTUM ELECTRONICS

A. OPERATING CHARACTERISTICS OF A $\text{MgF}_2\text{:Ni}$ LASER

A $\text{MgF}_2\text{:Ni}$ laser at 35 K has been operated in the 1.6- to 1.7- μm region with 1.7 W of CW output power, an absorbed pump power conversion efficiency of 37 percent, and an absorbed pump power threshold of 50 mW. Damped relaxation oscillations leading to true CW operation and lasing up to a crystal temperature of 200 K have been observed.

The 1.95-cm-long laser crystal, doped with 0.4-percent Ni, was pumped longitudinally by a 1.33- μm CW Nd:YAG laser. The ends of the crystal were polished and coated to form a laser cavity. The pump entrance face was flat and coated for high reflectivity from 1.6 to 1.75 μm ; the opposite face had a 2.0-cm radius of curvature and was coated for ~ 0.4 -percent transmission at 1.64 μm . The crystal was held in a conventional liquid nitrogen (LN_2) Dewar or in a helium gas-cooled variable-temperature Dewar, depending on the experiments.

Fig. II-1. Threshold absorbed pump power P_{TH} and operating wavelength λ vs crystal temperature T .

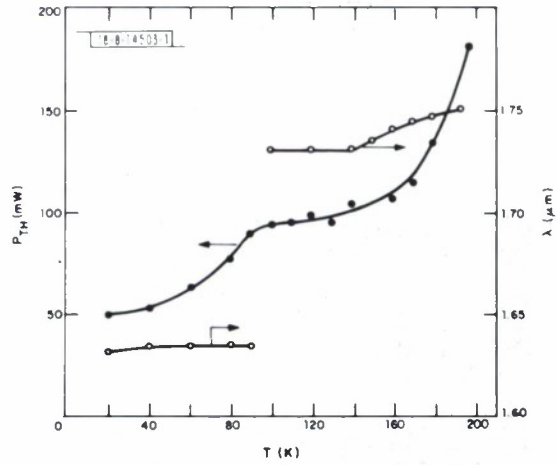


Figure II-1 shows the variation in threshold observed as the crystal temperature was raised from 20 to 200 K. The TEM_{00} pump laser output was focused to a beam radius of $\sim 220 \mu\text{m}$ in the crystal. Also shown in the figure is the laser operating wavelength, the temperature variation of which is similar to previous observations and is explained in terms of local maxima in the gain-vs-wavelength curve for $\text{MgF}_2\text{:Ni}$ (Ref. 1). The maximum operating temperature was limited by the output of the pump laser, and operation at higher temperatures should be possible.

By chopping the pump laser beam, it was possible to observe damped relaxation oscillations which yielded information on the laser cavity losses. Figure II-2(a-d) shows examples of the oscillations observed. The oscillation frequency ω for long times, i.e., the linear region of oscillation, is approximately related to the total round-trip cavity loss L by the equation

$$L = \frac{\tau \tau_{\text{rt}} \omega^2}{\rho - 1}$$

where τ is the spontaneous lifetime, τ_{rt} is the cavity round-trip time, and ρ is the ratio of pump power to threshold pump power. The equation is valid for the case of a Gaussian pump

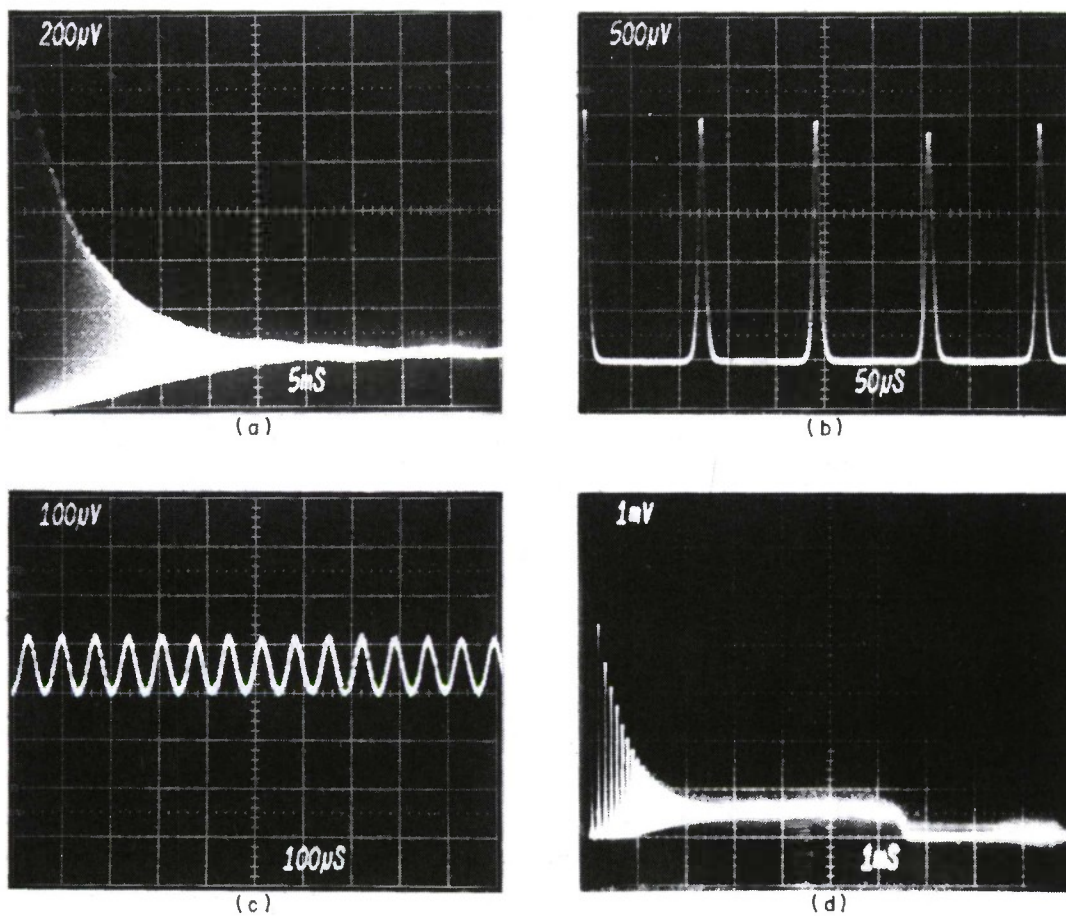
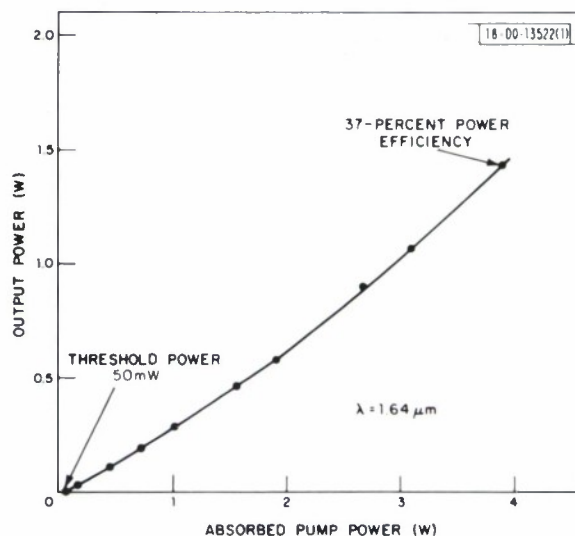


Fig. II-2. Relaxation oscillations in $\text{MgF}_2\text{:Ni}$ laser output: (a) envelope of oscillations at $T = 20 \text{ K}$, $\rho = 2.1$; (b) initial spiking at start of oscillations; (c) linear regime; (d) envelope at $T > 77 \text{ K}$, $\rho = 1.4$.

beam cross section,² and is a reasonable approximation to the actual condition of longitudinal pumping in the experiments since the pump beam was not strongly absorbed. At $T = 20$ K, the cavity loss was calculated from the data to be 1.6 percent, while in the LN_2 Dewar with $T > 77$ K the loss was 2.5 percent. Power-output-vs-input measurements with TEM_{00} operation of the pump laser yielded slope efficiencies of 26 and 21 percent at $T = 20$ K and in the LN_2 Dewar, respectively, which is to be compared with values of 20 and 13 percent calculated assuming an output mirror transmission of 99.6 percent. Given the uncertainties in the measurements, especially in how much power was absorbed by the crystal, such discrepancies are not unreasonable. The laser cross section, calculated knowing the threshold pump intensity and cavity loss, is $2.4 \times 10^{-21} \text{ cm}^2$, which is of the right order of magnitude given the spontaneous lifetime of 12 msec and fluorescent linewidth of $\sim 1000 \text{ cm}^{-1}$. Careful alignment of the pump laser to attain the damped oscillations shown in Fig.II-2 was required to avoid feedback between pump-laser and $\text{MgF}_2:\text{Ni}$ cavities; best results were obtained with considerable attenuation between the two cavities. We hope that YIG, which can have very low absorption at $1.33 \mu\text{m}$, can be used as a Faraday isolator to eliminate such feedback in later experiments.

The pump laser was capable of producing considerably higher output when allowed to oscillate in many transverse modes. To demonstrate the output power capability of the $\text{MgF}_2:\text{Ni}$ laser, the pump laser output was increased by initially using larger apertures in the pump-laser cavity and finally changing the cavity geometry. The curve shown in Fig.II-3 resulted, with $T = 35$ K at maximum absorbed power and with a total power conversion of 37 percent. Later experiments yielded 1.7 W of output at a lower conversion efficiency.

Fig.II-3. Output power vs pump power with multimode pump laser.



Experiments to obtain continuous tuning of the $\text{MgF}_2:\text{Ni}$ laser are being planned and will employ external cavities. In particular, it is possible to place a Brewster angle crystal in a three-mirror astigmatically compensated cavity³ such that pump thresholds below 100 mW can be achieved, and tuning can be done with birefringent elements.

P. F. Moulton
A. Mooradian

B. MINI-TEA CO₂ LASER

In our previous report,⁴ we discussed the construction and operation of a mini-TEA CO₂ laser which has a volume energy extraction comparable to larger, conventional TEA lasers. In this report, we describe design improvements intended to help achieve operation at high pulse repetition frequencies (PRF). In addition, we report obtaining 20 mJ of output in the TEM₀₀ mode and 18-percent average conversion efficiency in frequency-doubling experiments.

We previously noted⁴ that the repetition rate was limited to about 10 Hz, with arcing between electrodes occurring at higher PRF. A major reason for this limitation was the use of a longitudinal gas flow in the laser, with both the inlet and outlet on the same side of the Rogowski electrodes. This geometry was necessitated by the preionizing sparkboard, which prevented transverse gas flow. In addition, we observed during the present period that the effectiveness of the sparkboard as a preionization source deteriorated rapidly at high repetition rates, due to the buildup of carbon deposits at the spark locations.

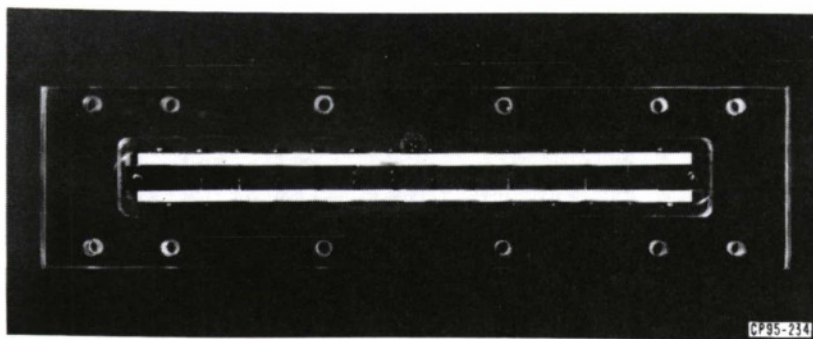


Fig.II-4. Spark-pin preionization unit.

To overcome these problems, the spark-pin assembly shown in Fig.II-4 was designed and built to replace the sparkboard. The assembly consists of two partially copper-plated boron nitride boards and a series of copper-tungsten electrode pins soldered to the plating. The electrode spacing is set by the brass endpieces, which also serve as electrical contacts. To obtain a transverse flow with the spark-pin assembly, two holes drilled in the lucite plate behind the pins served as joint inlets while the original inlet and outlet on the opposite plate were attached together to serve as outlets. With this arrangement, a 40-Hz PRF was achieved before the onset of arcing. This represents a fourfold increase over previous results; we believe that an arrangement involving a smooth flow over the entire electrode area will lead to significant further improvement. No degradation effects have been observed with the first spark-pin unit as yet.

In addition to a mini-TEA laser fired by a triggered spark gap, we have constructed a second unit fired by a hydrogen thyatron. The advantages of the thyatron over the spark gap are more reliable firing, an order-of-magnitude reduction in jitter between triggering and firing, and a higher ultimate PRF for the system.

The spark-gap-fired mini-TEA laser has reached pulse output levels up to 44 mJ, corresponding to an energy extraction near 25 J/liter. The highest output obtained thus far with the thyatron-fired unit has been slightly under 40 mJ. We believe this difference is due to slightly more inductance in the thyatron circuit. The current pulse in the thyatron-fired circuit has a width (FWHM) of 100 nsec.

Using a pair of intracavity variable apertures, we obtained TEM_{00} pulses of 20 mJ. In general, we found that about half the pulse energy obtained without aperturing was available in the TEM_{00} mode.

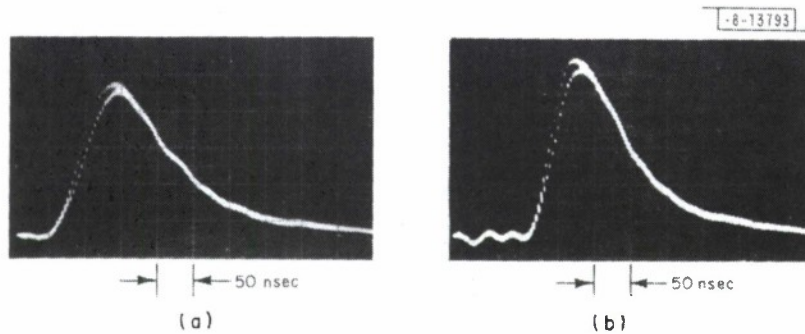


Fig. II-5. (a) Mini-TEA CO_2 laser output pulse (TEM_{00}); (b) frequency-doubled pulse.

Preliminary frequency-doubling experiments with the output of a mini-TEA laser operating in the TEM_{00} mode incident upon a $CdGeAs_2$ crystal were carried out, and resulted in average pulse energy conversion efficiencies of up to 18 percent. Saturation effects were present in these experiments since the increase in conversion efficiency with increasing input energy was found to be less than linear. The $He:N_2:CO_2$ flowing-gas ratio used for frequency doubling was 7:0.8:1, with the N_2 component reduced to minimize the pulse tail. Typical mini-TEA laser and second-harmonic pulses are shown in Figs. II-5(a) and (b), respectively. The FWHM of the laser pulse is nearly 150 nsec with a total energy of 11.8 mJ, while that of the frequency-doubled pulse is about 100 nsec at a total energy of 2.1 mJ. The presence of partial longitudinal mode locking at 3×10^8 Hz can be seen in both figures.

N. Menyuk
P. F. Moulton

C. NONLINEAR INFRARED PROCESSES IN CRYOGENIC LIQUIDS

We have observed four-wave sum-and-difference-frequency generation of the outputs of two CO_2 TEA lasers in liquid $CO-O_2$ mixtures at 77 K. The efficiencies of these processes are enhanced by a two-photon resonance with the CO vibrational mode. We have studied both the polarization dependence and the lineshape of the two-photon resonance, and have also measured the mixing efficiencies. The efficiency of the sum-frequency generation process is comparable to the third-harmonic generation efficiency. The measured efficiency of 0.1 percent of the difference-frequency generation process is somewhat lower due to differences in the Manley-Rowe factors and in the maximum values for the phase mismatch integrals. In addition to using anomalous dispersion for phasematching,^{5,6} we have also employed noncollinear phasematching for difference-frequency generation. Since the details of this work are described in a paper to be published shortly,⁷ they will therefore not be repeated here.

We have also examined theoretically the possibility of frequency-tripling CO_2 laser radiation in a molecular system composed of SF_6 dissolved in liquid argon. The ν_3 mode of SF_6 is at 939.6 cm^{-1} , and the linewidth is only 0.5 cm^{-1} . It is therefore possible to choose a CO_2 pump line [P(28) at 936.8 cm^{-1}] which is in two-photon resonance with the SF_6 first overtone transition,

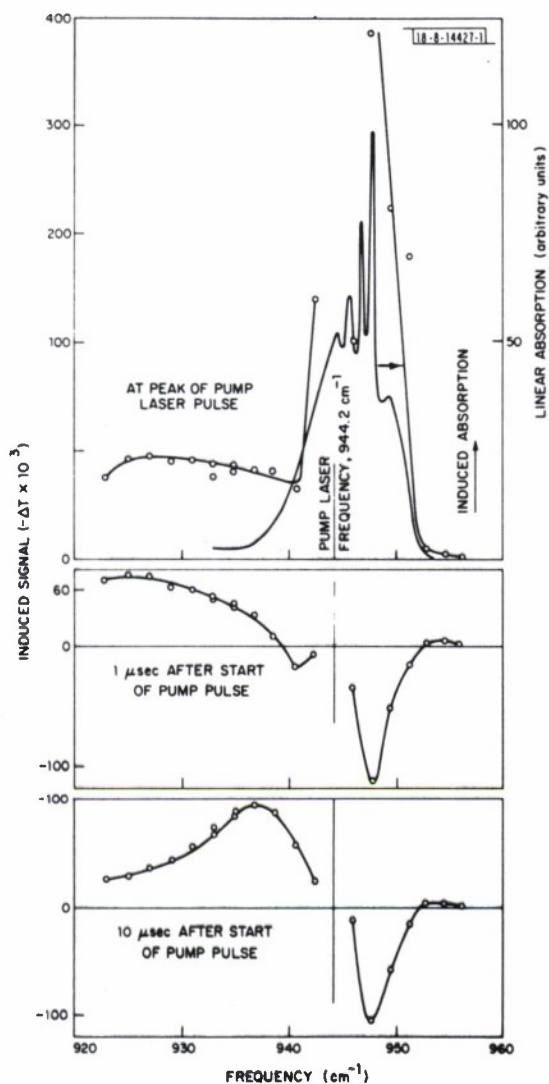


Fig.II-6. Spectral evolution of double-resonance signals observed for 0.05 Torr of SF_6 with pump laser intensity of 2.6 MW/cm^2 at 944.2 cm^{-1} .

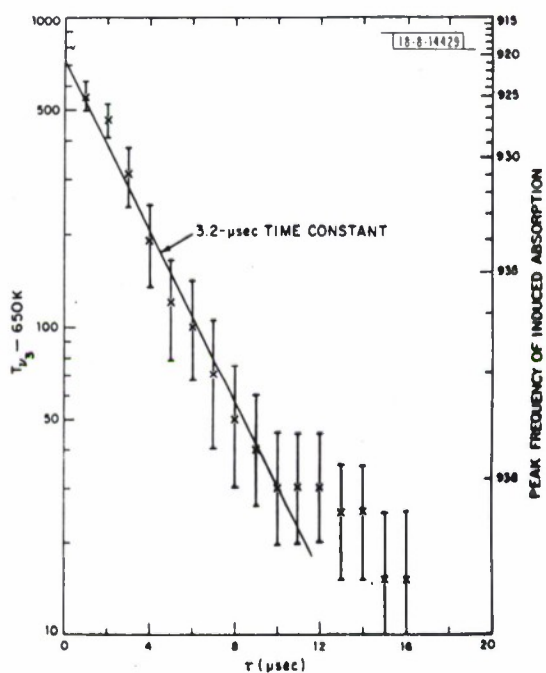


Fig.II-7. Time dependence of ν_3 -mode temperature for excitation of 2.6 MW/cm^2 at 944.2 cm^{-1} . Corresponding peak induced-absorption frequencies are also shown.

although it falls outside the SF_6 fundamental absorption band. The calculated third-order susceptibility is $\chi^{(3)} = 2 \times 10^{-34} \text{ Asm/V}^3$ for a density of $3.5 \times 10^{16} \text{ cm}^{-3}$ of SF_6 dissolved in the liquid. For efficient frequency conversion, it is probably necessary to dissolve about $3 \times 10^{18} \text{ molecules/cm}^3$ of SF_6 . By choosing two isotopes of SF_6 , $^{32}\text{SF}_6$ together with $^{33}\text{SF}_6$ or $^{34}\text{SF}_6$, the dispersion can easily be optimized for third-harmonic generation (the ν_3 modes of $^{33}\text{SF}_6$ and $^{34}\text{SF}_6$ are at 930.8 and 922.6 cm^{-1} , respectively). At the outset this appeared to be a promising scheme; however, linear absorption in SF_6 will limit the efficiency since the calculated absorption constant at the pump wavelength is 5 cm^{-1} at a SF_6 density of $3 \times 10^{18} \text{ cm}^{-3}$.

H. Kildal
S.R.J. Brueck

D. COLLISIONLESS INTRAMOLECULAR ENERGY TRANSFER IN VIBRATIONALLY EXCITED SF_6

The demonstration of multiphoton laser isotope separation in SF_6 has led to numerous experimental and theoretical studies of the dissociation and energy absorption processes.⁸⁻¹¹ It has been hypothesized that, after several initial, isotopically selective transitions, the absorption process occurs in a "quasi-continuum" where the detailed level structure of the SF_6 molecule has been spread out due to intramolecular energy transfer processes and the very high density of states. Within this quasi-continuum, collisionless intramolecular energy transfer results in a thermalization of the internal vibrational energy of the molecule among all the vibrational modes. While the evidence suggests that, near the dissociation limit, intramolecular energy transfer occurs on a nanosecond or faster time scale, no direct measurements of this time have been made. Neither has it been fully appreciated that the time scale of this intramolecular energy thermalization must be a strong function of excitation level, ranging from a sub-nanosecond time scale for a molecule excited to a nearly dissociative level to an essentially infinite time scale for molecules with only a single vibrational quantum above the ground state.

We previously reported (see p. 21 in Ref. 4) on the use of infrared-infrared double-resonance measurements to obtain the spectral dependence of the induced absorption in CO_2 laser-excited SF_6 . We have now analyzed the time dependence of the induced absorption spectra using a simple model which allows us to obtain a measure of the collisionless intramolecular energy transfer time.

Figure II-6 shows the spectrum of the induced signal at various times after the CO_2 P(20) pump pulse; the spectra were obtained using a line-tunable CO_2 laser to probe the ν_3 -mode absorption. At $10 \mu\text{sec}$ after the pump pulse, the peak of the induced absorption spectrum on the red side of the pump has shifted to higher frequencies, indicating that the initially highly excited ν_3 -mode population is relaxing down the ν_3 ladder. These spectra were only very weakly dependent on SF_6 pressure over the range from 0.01 to 0.05 Torr , indicating a collisionless relaxation mechanism.

It is frequently useful to describe the vibrational excitation of an ensemble of polyatomic molecules by assigning temperatures to the various vibrational modes of the molecule. Nowak and Lyman¹² measured the absorption spectrum of the ν_3 band of SF_6 at high temperatures and demonstrated a simple monotonic relationship between the temperature and the wavelength of peak absorption. This allows us to obtain a correlation between our measured spectra and the ν_3 -mode temperature, T_{ν_3} . The time dependence of the quantity $(T_{\nu_3} - 650 \text{ K})$ is plotted on a semilog scale in Fig. II-7. The final temperature of 650 K was obtained from an independent

calculation¹³ of the vibrational temperature of thermally equilibrated SF_6 with an average excess vibrational energy of 3 photons/molecule, the value obtained from acoustic measurements¹¹ of energy deposition for 2.6 J/cm², 100 nsec, P(20) TEA laser pulses. Figure II-7 shows a simple exponential dependence of the ν_3 -mode temperature with a time constant of 3 ± 1 μsec for the ν_3 -mode vibrational energy to equilibrate with the remaining vibrational modes of the SF_6 molecule. There is good agreement between the calculated 650 K equilibrium temperature and the long time limit of the ν_3 -mode temperature deduced from the spectra. The initial ν_3 -mode temperature obtained from Fig. II-7 is 1375 K, which is somewhat lower than the 1950 K which we estimate[†] from the heat capacity of the triply degenerate ν_3 mode alone. However, putting in the calculated 1950-K initial ν_3 -mode temperature changes the time constant only slightly, to about 2 μsec .

Because the observed time dependences of the double-resonance signals over a range of probe frequencies are essentially pressure independent for a decade variation in pressure, and since the low excitation collisional $\nu_3 \rightarrow \nu_4$ vibrational equilibration time ranges from 150 to 15 μsec over this pressure range,¹⁴ we conclude that we have observed collisionless intramolecular energy transfer on a microsecond time scale. This time scale is expected to be a very rapid function of excitation level; a systematic extension of these experiments as a function of excitation intensity should provide a very interesting map of intramolecular vibrational energy flow within complex molecules.

S. R. J. Brueck
T. F. Deutsch

[†] Estimated from $\langle n \rangle = 3 (e^{\hbar\omega/kT} - 1)^{-1}$.

REFERENCES

1. L. F. Johnson, H. J. Guggenheim, and R. A. Thomas, Phys. Rev. 49, 179 (1966).
2. S. R. Chinn, private communication.
3. H. Kogelnik, E. P. Ippen, A. Dienes, and C. V. Shank, IEEE J. Quantum Electron. QE-8, 373 (1972).
4. Solid State Research Report, Lincoln Laboratory, M.I.T. (1977:3), p.17.
5. H. Kildal and S. R. J. Brueck, Phys. Rev. Lett. 38, 347 (1977), DDC AD-A042238/6.
6. S. R. J. Brueck and H. Kildal, Opt. Lett. (to be published).
7. H. Kildal and S. R. J. Brueck, Appl. Phys. Lett. (to be published).
8. R. V. Ambartzumian, Yu. A. Gorokhov, V. S. Letokhov, and G. N. Makarov, JETP Lett. 21, 171 (1975).
9. R. V. Ambartzumian, in Tunable Lasers and Applications, A. Mooradian, T. Jaeger, and P. Stokseth, Eds. (Springer-Verlag, New York, 1976), p. 150.
10. D. M. Larsen and N. Bloembergen, Opt. Commun. 17, 254 (1976).
11. J. G. Black, E. Yablonovitch, N. Bloembergen, and S. Mukamel, Phys. Rev. Lett. 38, 1131 (1977).
12. A. V. Nowak and J. L. Lyman, J. Quant. Spectrosc. Radiat. Transfer 15, 945 (1975).
13. D. R. Stull and H. Prophet, JANEF Thermochemical Tables, NSRDS-NBS37 (U.S. National Bureau of Standards, Washington, D.C., 1971).
14. R. D. Bates, J. T. Knudtson, G. W. Flynn, and A. M. Ronn, Chem. Phys. Lett. 8, 103 (1971).

III. MATERIALS RESEARCH

A. SIMPLIFIED FABRICATION OF GaAs HOMOJUNCTION SOLAR CELLS WITH INCREASED CONVERSION EFFICIENCIES

We recently reported¹ the development of shallow-homojunction single-crystal GaAs solar cells, fabricated without the use of $\text{Ga}_{1-x}\text{Al}_x\text{As}$ layers, with conversion efficiencies as high as 15.3 percent at AM 1. These cells employ an $n^+/p/p^+$ structure prepared by chemical vapor deposition (CVD), in which surface recombination losses are reduced because the n^+ layer is so thin that most of the carriers are generated in the p layer below the junction. We have now obtained conversion efficiencies as high as 20 percent for shallow-homojunction cells, close to the value of 22 percent reported² for the best $\text{Ga}_{1-x}\text{Al}_x\text{As}/\text{GaAs}$ heterostructure cells. The improved cells, which are fabricated by a simplified technique that does not require any vacuum-processing steps, utilize a somewhat thinner n^+ layer and an antireflection coating prepared by anodic oxidation of the n^+ layer.

In our earlier cells,¹ the n^+ layer was 1300 Å thick and the antireflection coating consisted of successive layers of SiO and MgF_2 . In an initial attempt to increase the efficiency, the thickness of the n^+ layer was reduced to 600 to 700 Å, and the antireflection coating was prepared by electron-beam evaporation of TiO_2 and MgF_2 . Efficiencies of 13 to 14 percent were obtained for uncoated cells, but coated cells had lower efficiencies because their open-circuit voltage was reduced by 10 to 15 percent. This decrease in open-circuit voltage may have resulted from degradation of the GaAs during deposition of the coating (perhaps due to soft x-rays generated during electron-beam evaporation) or from stress on the junction produced by the coating. To eliminate such effects, we developed the following procedure for preparing the antireflection coating by anodic oxidation of the n^+ layer.

The electrolyte solution used for anodization, which is similar to the one described by Hasegawa and Hartnagel,³ is prepared by mixing 3 g of tartaric acid with 100 ml of H_2O , adding sufficient NH_4OH to adjust the pH to about 6.2, and then adding 250 ml of propylene glycol. The final pH is 5.6 to 5.8. Anodization of the GaAs is performed at room temperature using a platinum wire as cathode. In experiments on n^+ GaAs wafers as large as 5 cm in diameter, we found that anodic layers of uniform thickness can be obtained by using a constant-current source with a voltage limiter instead of using a constant-voltage source. The source is set at a current corresponding to a current density of about $750 \mu\text{A}/\text{cm}^2$ for the GaAs anode, and the maximum output voltage is set at about 43 V. The current initially remains constant until the voltage increases to its limiting value, after which the voltage remains constant and the current decreases. The growth rate of the anodic layer is about $20 \text{ Å}/\text{V}$ and does not depend strongly on current density. Anodization is terminated when the current falls to one-tenth of its initial value. The layer produced by the process, which takes less than 5 min., is about 850 Å thick, and the thickness of GaAs consumed is about 550 Å. The anodic layer is stable up to at least 250°C in air. The optical constants were measured by ellipsometry at 4358 and 5461 Å using a Hg lamp, and at 6328 Å using a He-Ne laser. The refractive indices found at these wavelengths are 1.91, 1.85, and 1.83, respectively, in qualitative agreement with the values just reported by Ishii and Jeppsson⁴ for anodic layers prepared on GaAs by a similar technique.

The GaAs layers used in the improved cells, like those in the earlier devices, were grown in an $\text{AsCl}_3\text{-Ga-H}_2$ CVD system on p^+ Zn-doped (100)-oriented substrates with a carrier

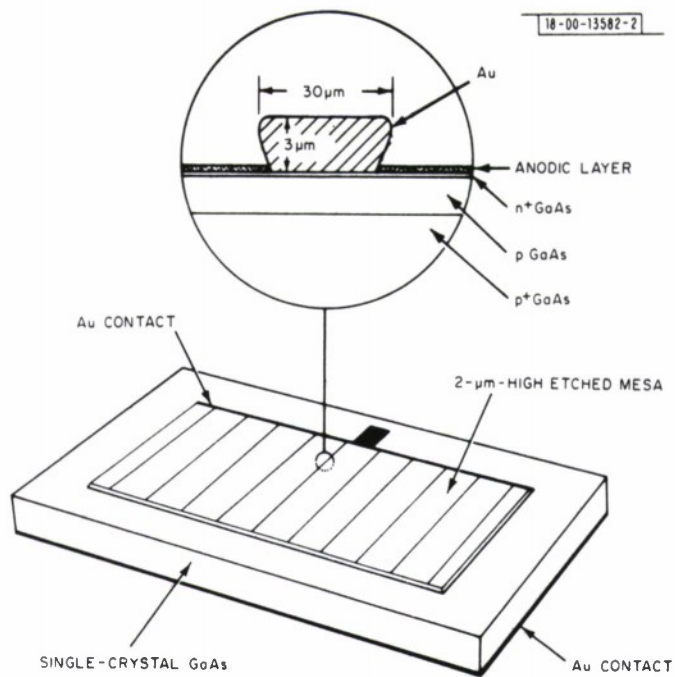


Fig.III-1. Schematic diagram of single-crystal GaAs shallow-homojunction solar cell with anti-reflection coating prepared by anodic oxidation.

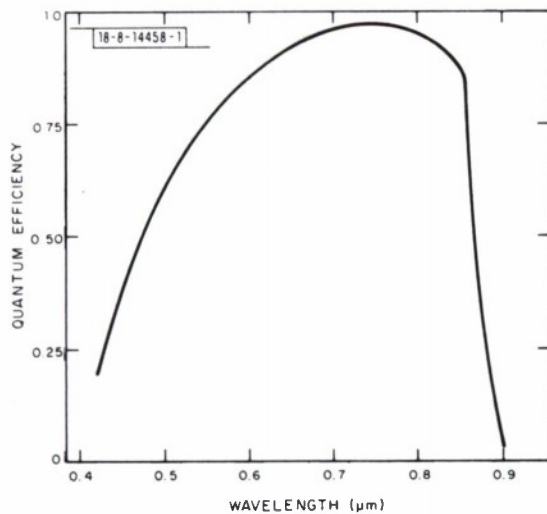


Fig.III-2. Quantum efficiency as a function of wavelength for GaAs shallow-homojunction solar cell with 20-percent conversion efficiency at AM 1.

concentration of 10^{18} cm^{-3} . A p layer about $3 \mu\text{m}$ thick was first grown on the substrate, followed by an n^+ layer about 1000 \AA thick. The p layer ($p \sim 10^{16} \text{ cm}^{-3}$) and n^+ layer ($n \sim 5 \times 10^{18} \text{ cm}^{-3}$) were doped with Zn and S, respectively, by using $(\text{C}_2\text{H}_5)_2\text{Zn}$ and H_2S sources. Following GaAs growth, the n^+ layer was anodically oxidized by the process described above, and a layer of Au about $3 \mu\text{m}$ was electroplated on the p^+ substrate as the back contact. Photoresist AZ 1350J was spun on the anodic layer, and photolithographic techniques were used to etch openings for ohmic contact fingers in the anodic layer. For each cell there were 10 openings, 0.5 cm long and $25 \mu\text{m}$ wide, spaced 1 mm apart. A layer of Au about $3 \mu\text{m}$ thick was then electroplated into the openings, and the wafer was annealed under flowing N_2 for 1 sec at 300°C on a graphite heater strip to produce ohmic contact between the Au fingers and the n^+ layers. Finally, the active area of the cell was defined by etching a $1 \times 0.5\text{-cm}$ rectangular area in the GaAs. A schematic diagram of the cell, including an expanded cross-sectional view of one of the contact fingers, is shown in Fig. III-1.

Efficiency measurements, using a high-pressure Xe lamp with a water filter as a simulated AM 1 source, were made on 5 cells fabricated from wafers with p and n^+ layers differing slightly in carrier concentration. The incident intensity was adjusted to 100 mW/cm^2 , using a NASA-measured GaAs solar cell as a reference. All these cells have efficiencies between 18 and 20 percent. The best cell was also measured on a roof at Lincoln Laboratory at an ambient temperature of about 20°C . The solar flux density measured with a pyranometer was 98 mW/cm^2 , close to AM 1 conditions. The open-circuit voltage was found to be 0.97 V , the short-circuit current 25.6 mA/cm^2 , and the fill factor 0.81, giving a measured conversion efficiency of 20.5 percent. The quantum efficiency of this cell as a function of wavelength is shown in Fig. III-2. The quantum efficiency exceeds 90 percent at the maximum, but it decreases strongly at shorter wavelengths, indicating that surface recombination effects are still significant.

J. C. C. Fan R. L. Chapman
C. O. Bozler R. W. McClelland

B. CHEMISORBED PHASES OF O_2 ON TiO_2 AND SrTiO_3

The electronic properties of TiO_2 (rutile) and SrTiO_3 surfaces have recently received considerable attention because these materials are used as catalytic electrodes in the decomposition of water by photoelectrolysis. Ultraviolet photoemission spectroscopy (UPS) studies^{5,6} have shown that vacuum-fractured surfaces of both materials have the stoichiometry of the bulk, with the surface Ti ions in a $\text{Ti}^{4+} (3d^0)$ configuration. Only weak emission is seen from the bandgap region, presumably associated with a small density of residual surface defects. Ar-ion bombardment disorders the surfaces and removes O (and also Sr from SrTiO_3), leaving surface Ti ions in a $\text{Ti}^{3+} (3d^1)$ configuration. The d-electrons associated with the Ti^{3+} ions give rise to a band of surface states within the bulk bandgap. It is presumably these states that are important catalytic sites in photoelectrolysis.

We previously reported a UPS study of the chemisorption of H_2O on TiO_2 and SrTiO_3 surfaces.⁷ We have now extended this study to the chemisorption of O_2 on these materials. Several adsorbed phases are found. The same initial phase, which we believe to consist of O_2^{2-} ions, is present on all surfaces for low O_2 exposures.

Single-crystal samples of TiO_2 and SrTiO_3 were reduced in vacuum, giving a bulk carrier concentration of about $10^{19} \text{ electrons/cm}^3$. The sample surfaces were prepared either by fracturing in vacuum, which yielded roughly TiO_2 (110) and SrTiO_3 (100) surfaces, or by orienting

and polishing followed by 500-eV Ar-ion bombardment in the ultra-high vacuum system. After ion bombardment, some samples were annealed at about 1100 K. The various surfaces were subjected to O_2 exposures ranging from 0.5 to 10^8 L ($1 \text{ L} \equiv 10^{-6}$ Torr-sec). Photoemission was excited by He (I) radiation (21.2 eV), and UPS spectra were measured with a double-pass cylindrical-mirror electron spectrometer (0.2-eV resolution).

Figure III-3 shows a family of UPS spectra for Ar-ion-bombarded $SrTiO_3$ (100) before exposure to O_2 (0 L) and after exposures of 0.5 to 10^8 L. The spectra have been aligned by setting $E_v \equiv 0$; positive initial energies represent electron states located below the top of the valence band. Emission from the valence band extends from 0 to 6 eV, and emission from the d-electron surface-state band extends from about -1 to -4 eV. The steep rise beyond 6 eV is due to inelastically scattered electrons. Two distinct adsorbed phases are formed when the surface is exposed to O_2 . The initial phase (I), with a sticking coefficient of 0.2 to 1, is obtained for exposures up to about 100 L. With increasing exposure, the emission in the valence-band region increases, while the emission for $E < 0$ decreases, showing that the bandgap surface states are depopulated. The spectrum for phase I can be seen in Fig. III-4(a), which shows the difference between the spectrum of Fig. III-3 for 30-L exposure, where phase I is complete, and that for the clean surface. Above 100 L a second phase (II) appears, characterized by a third peak below the valence band (7 to 8 eV) and by changes in the relative heights of the peaks in the valence-band region. If we assume that phase I remains when phase II is adsorbed, we can obtain the characteristic spectrum for phase II by subtracting the spectrum for 30-L exposure from that for 10^8 L. The difference spectrum obtained in this manner is shown in Fig. III-4(b).

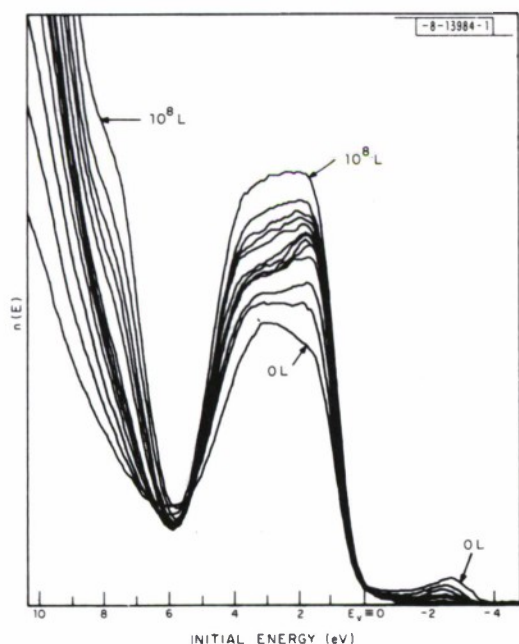


Fig. III-3. UPS spectra (using 21.2-eV photons) for Ar-ion-bombarded $SrTiO_3$ (100) after successive exposures to O_2 ($1 \text{ L} \equiv 10^{-6}$ Torr-sec).

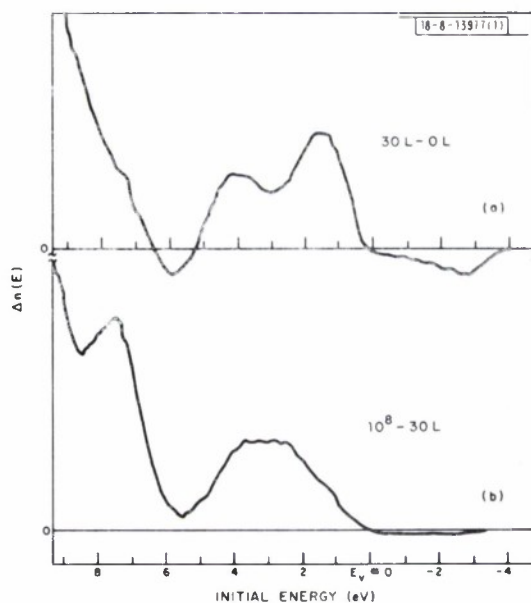


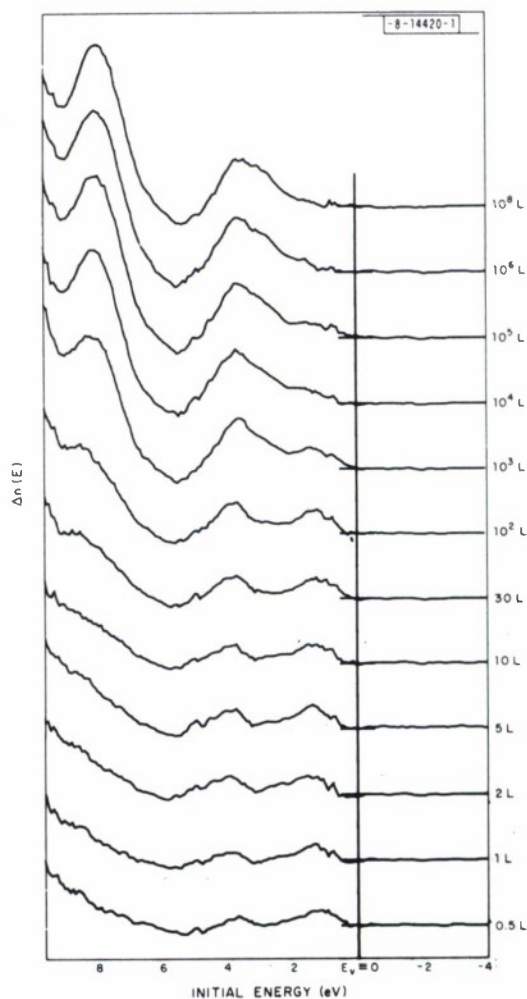
Fig. III-4. UPS difference spectra for Ar-ion-bombarded $SrTiO_3$ (100). (a) Phase I (30 - 0 L); (b) phase II (10^8 - 30 L).

The spectrum for phase I [Fig. III-4(a)] resembles the portion of the UPS spectrum for clean, ordered SrTiO_3 surfaces (i.e., vacuum-fractured or annealed) that is due to emission from the valence band.⁶ Both spectra exhibit emission from 0 to 6 eV, and both have two peaks with about the same separation in that region. (These peaks are smeared together for the disordered surface shown in Fig. III-3.) Since the valence band in SrTiO_3 arises primarily from O^{2-} ions, the similarity of the spectra strongly suggests that phase I consists of adsorbed O^{2-} ions. The depopulation of the bandgap surface states during the formation of phase I indicates a transfer of electrons from the surface to the adsorbate.

The spectrum for phase II [Fig. III-4(b)] has a broad peak (which may consist of two unresolved peaks) in the valence-band region and another peak at 7 to 8 eV. We have not been able to identify the adsorbed species in phase II. It is probably not neutral O_2 , since the free molecule has a four-peaked UPS spectrum;⁸ however, we cannot rule out a severely perturbed neutral O_2 molecule. The species is probably some charged state of either O or O_2 , but no gas-phase UPS spectra of such species are available for comparison.

Figure III-5 shows a series of difference spectra, obtained by subtraction of the spectrum for a clean surface, for a vacuum-fractured SrTiO_3 (100) surface exposed to O_2 . Two adsorbed

Fig. III-5. UPS difference spectra for vacuum-fractured SrTiO_3 after successive exposures to O_2 .



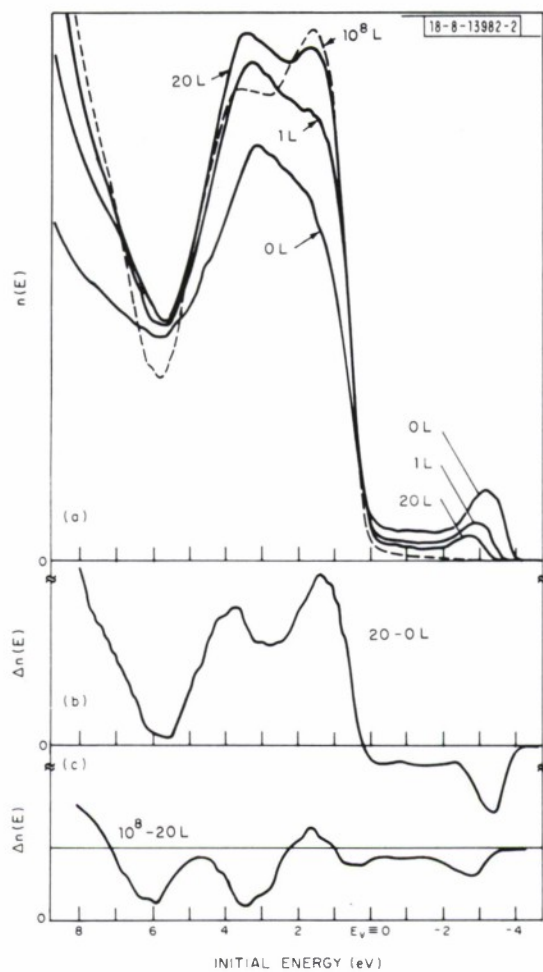


Fig. III-6. (a) UPS spectra for Ar-ion-bombarded TiO_2 after various exposures to O_2 ; (b) UPS difference spectrum for phase I ($20 - 0$ L); (c) UPS difference spectrum for ($10^8 - 20$ L).

phases are present here also. The spectra for phase I are almost identical to those for ion-bombarded SrTiO_3 (100) surfaces [Fig. III-4(a)]; we again interpret this phase as consisting of adsorbed O^{2-} ions. (Since there are essentially no bandgap surface states on clean, vacuum-fractured surfaces,⁶ the amplitude of the difference spectra is zero in the bandgap region.) For exposures greater than 10^4 L, the same peak below the valence band appears as in Figs. III-3 and III-4, but the peak near 4 eV grows in amplitude at the expense of the peak near 1 eV; the latter has completely disappeared at 10^8 L. This indicates that phase I is no longer present. That this is indeed the case is also indicated by the similarity between the total difference spectrum for 10^8 L in Fig. III-5 and the spectrum for phase II alone in Fig. III-4(b). The spectra for vacuum-fractured and for ion-bombarded SrTiO_3 are therefore consistent with the conclusion that the same two adsorbed phases exist on both surfaces, but that phase II is adsorbed in addition to phase I on bombarded surfaces while it is adsorbed in place of phase I on fractured surfaces.

Ar-ion-bombarded SrTiO_3 surfaces that have subsequently been annealed are well ordered (i.e., exhibit good LEED patterns) but remain O- and Sr-deficient, and the bandgap photoemission peak is still observed.⁶ These annealed surfaces exhibit only one adsorbed phase upon exposure to O_2 . This phase is complete after 5- to 10-L exposure, with no significant changes in the spectra for subsequent exposures. The spectra for this phase differ in shape from those in Figs. III-4 and III-5, but they still contain two peaks in the valence-band region separated by 2.5 eV, and we believe that this phase also consists of O^{2-} ions. In the valence-band region of the UPS spectra, the changes resulting from O_2 exposure are smaller in amplitude for annealed SrTiO_3 than for fractured or bombarded surfaces. There appear to be fewer adsorption sites on annealed SrTiO_3 surfaces, and none of those seem to be favorable for phase II adsorption.

The only TiO_2 surfaces for which we have studied O_2 adsorption in detail are Ar-ion-bombarded surfaces; UPS spectra for several O_2 exposures are shown in Fig. III-6(a). Two adsorbed phases also are found here. The first one, whose difference spectrum is shown in Fig. III-6(b) for 20-L exposure, exhibits the same type of two-peaked structure in the valence-band region as that seen for SrTiO_3 . The peaks are again separated by 2.5 eV, indicating that this phase too consists of O^{2-} ions. Exposure to O_2 depopulates the bandgap surface states in TiO_2 , but at a much slower rate than for SrTiO_3 ; the emission due to those states is only reduced by about a factor of three for the exposure where the first adsorbed phase becomes complete (20 L), and 10^5 - to 10^8 -L O_2 are necessary to completely depopulate the states.

For exposures above about 10^3 L, additional changes occur in the valence-band region of Ar-ion-bombarded TiO_2 that are entirely different from those seen for SrTiO_3 . Figure III-6(c) shows the difference spectrum for ($10^8 - 20$ L); since most of this spectrum is negative, no simple addition of a second phase is taking place. The difference spectrum for ($10^8 - 0$ L) looks very much like Fig. III-6(b), however, with only relative changes in the heights of the two peaks and no trace of the peak at 7 to 8 eV seen in Figs. III-3 through III-5 for SrTiO_3 ; thus, no readily distinguishable second phase appears to replace the first phase. We have not yet been able to determine the nature of the adsorbed phase (or phases) for large O_2 exposures.

V. E. Henrich
G. Dresselhaus†
H. J. Zeiger

† National Magnet Laboratory, M.I.T.

REFERENCES

1. C. O. Bozler and J. C. C. Fan, Appl. Phys. Lett. 31, 629 (1977).
2. J. M. Woodall and H. J. Hovel, Appl. Phys. Lett. 30, 492 (1977).
3. H. Hasegawa and H. L. Hartnagel, J. Electrochem. Soc. 123, 713 (1976).
4. T. Ishii and B. Jeppsson, J. Electrochem. Soc. 124, 1784 (1977).
5. V. E. Henrich, G. Dresselhaus, and H. J. Zeiger, Phys. Rev. Lett. 36, 1335 (1976), DDC AD-A030621.
6. _____, Bull. Am. Phys. Soc., Ser. II 22, 364 (1977); and Solid State Commun. 24, 623 (1977).
7. _____, Solid State Commun. 24, 623 (1977); and Solid State Research Report, Lincoln Laboratory, M.I.T. (1977:3), p. 28.
8. D. W. Turner, C. Baker, A. D. Baker, and C. R. Brundle, Molecular Photoelectron Spectroscopy (Wiley-Interscience, New York, 1970), p. 52.

IV. MICROELECTRONICS

A. QUASI-OPTICAL MIXERS AT SUBMILLIMETER WAVELENGTHS

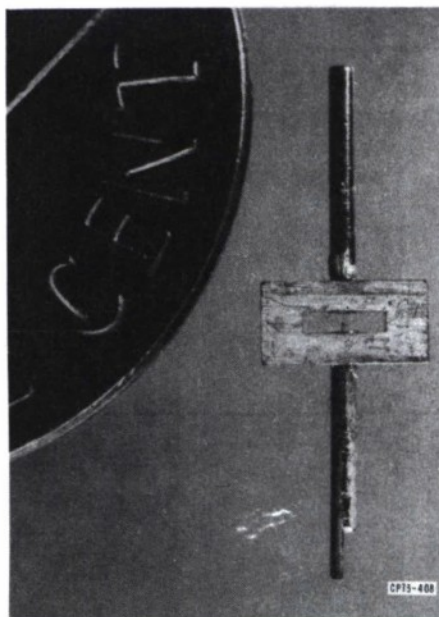
Techniques for building a quasi-optical mixer at submillimeter wavelengths are being investigated because of difficulties with the more conventional approach of embedding a diode in a fundamental waveguide at these frequencies. Two approaches are presently being pursued: a mixer insert to convert our standard diode-wafer package to fundamental guide, and a line source in a corner reflector. Both configurations are being modeled at X-band, and are also under construction for submillimeter operation.

1. Fundamental Waveguide Mixer

A single mode propagating in the vicinity of the whisker is not only desirable but is essential if efficient coupling and low-loss mixing are to be performed. The overmoded N-guide diode package (Fig. IV-1) suffers from several multimode-related problems when used in a submillimeter circuit environment. Energy propagating in some higher-order modes will not couple to the centrally located antenna whisker, and phase cancellation between several coupling modes considerably reduces the efficiency of the antenna. The multimoded beam pattern produced by the overmoded waveguide is not an efficient pattern to mate with beam-forming or focusing optics.

A fundamental waveguide environment surrounding the whisker/chip structure is an obvious technique to obtain the desirable single-mode characteristics. Unfortunately, in the submillimeter range of interest, fundamental waveguide having dimensions of 0.2 by 0.4 mm is not only

Fig. IV-1. Overmoded N-guide diode package.



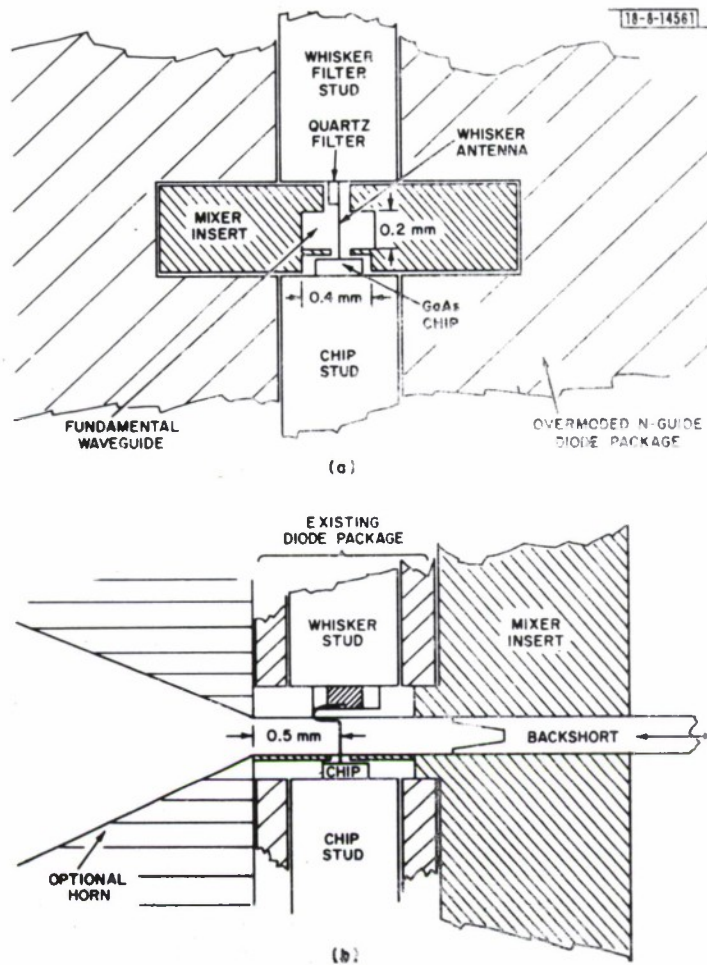


Fig.IV-2. Fundamental-waveguide-mixer insert. (a) Front view, and (b) side view (cross section).

lossy but would make diode packaging extremely difficult if each diode were to be packaged in fundamental waveguide. However, if we maintain the concept of packaging the diode in overmoded N-guide and use a fundamental-waveguide-mixer insert, we maintain the advantages of an interchangeable diode and at the same time can have the advantages of a fundamental-waveguide-mixer environment. Since only a few mixer mounts are required, expensive and difficult fabrication procedures can be employed to make the fundamental waveguide mixers – an approach that would be impractical if individual diodes were packaged in fundamental waveguide.

The concept of the fundamental-waveguide insert is shown in Fig. IV-2(a-b). The electroformed waveguide aperture (0.2×0.4 mm) surrounds the whisker stud. A slot 0.1 mm wide by 0.9 mm long enables the mixer to be inserted into the packaged diode around the whisker and quartz stripline filter. A cavity slot 0.4 mm wide by 0.1 mm high accommodates the GaAs chip. The length of the chip cavity slot will be determined experimentally. The sliding backshort will eventually be replaced by a fixed backshort for optimum low-loss performance. Since there is approximately one wavelength of fundamental guide between the throat of the horn and the whisker antenna, waveguide losses should be small, and suppression of higher-order modes should be adequate.

The first fundamental-waveguide-mixer inserts are being electroformed on polished aluminum mandrels. Subsequent inserts will be made using polished quartz mandrels on which a thin layer of gold has been evaporated or sputter deposited prior to electroforming. Mirror-finish, low-loss waveguide should result.

A 100X scale model of the mixer insert has been constructed for use with the 100X model of the overmoded N-guide package. Antenna patterns and impedance measurements have been made on this model, and the effects of chip cavity tuning and the whisker slots have been evaluated.

2. Line Source in a Corner Reflector

This approach¹ uses a long – typically four wavelengths – traveling-wave line source set in a corner reflector (Fig. IV-3). The line source is an extended point contact whisker, and the diode is mounted on the ground plane as shown. The parameters which are varied to control the radiation pattern and impedance characteristics are the length of the line source, the corner angle, and the separation between the line source and corner. This configuration is being investigated theoretically and experimentally with an X-band scale model.

By reciprocity, a basic requirement in the design of a quasi-optical mixer is that the radiated patterns efficiently illuminate the objective, i.e., the lens or reflector with which the device is to be used. Proper choice of the design parameters yields a pattern with a single mainlobe and low sidelobes which satisfy this requirement. The beam efficiency, defined as the ratio of the power intercepted by the objective from the mainlobe to the total power radiated, has been shown with model measurements to be greater than 80 percent.

A second basic requirement is that the terminal impedance be matched to the impedance presented by the diode. The terminal or radiation impedance is the impedance at the end of the wire that is attached to the diode. Model measurements show the impedance to have a resistive component between 100 and 200 ohms, and a reactive component less than 60 ohms over a wide (>40 percent) bandwidth. From our knowledge of the diode characteristics, this impedance level presents a reasonable match to the mixer diode. The signal frequency (as well as the local oscillator) is decoupled from the intermediate frequency port by about 13 dB. This is an inherent characteristic of a traveling-wave line source.

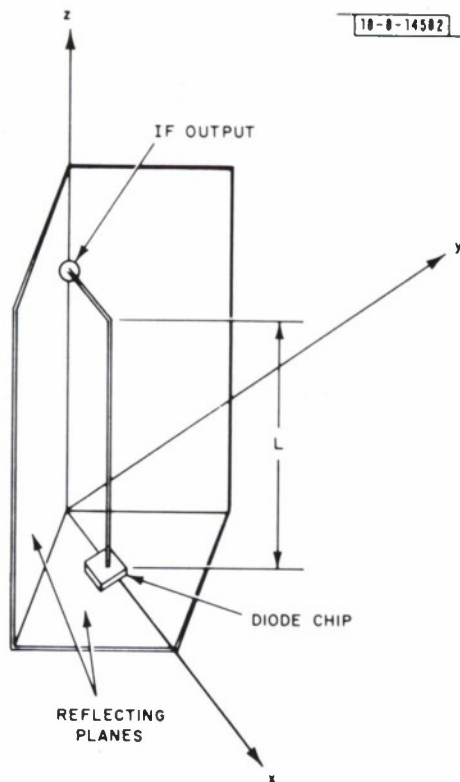


Fig. IV-3. Traveling-wave line source in corner reflectors.

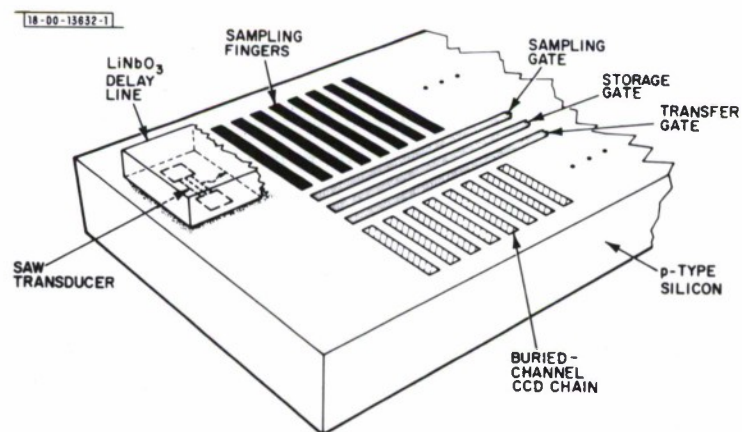


Fig. IV-4. Schematic view of SAW/CCD buffer memory device. Finger recharging components are not shown.

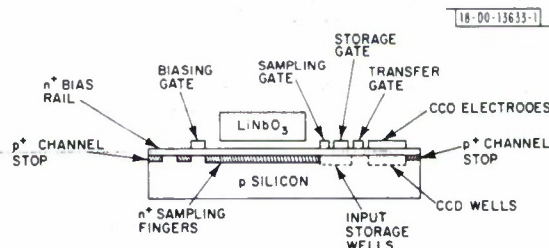
Antenna pattern and impedance measurements have been made at the model frequencies (6 to 8 GHz) for both types of mounts. These measurements have provided sufficient information for design and construction of the actual devices for operation at 600 to 800 GHz.

B. J. Clifton H. R. Fetterman
W. D. Fitzgerald P. E. Tannenwald
(Group 36)

B. CHARGE-COUPLED DEVICES: SAW/CCD BUFFER MEMORY

We have designed and are fabricating an integrated buffer memory having a surface-acoustic-wave (SAW) input and a CCD output. Exploratory work is being done with a 3.56- μ sec-long acoustoelectric interaction region operating at a 100-MHz center frequency with about a 30-MHz bandwidth. The device geometry used is shown in Figs. IV-4 and IV-5.

Fig. IV-5. Cross-sectional view of SAW/CCD buffer memory device.



The principles of device operation and typical operating parameters are expected to be as follows. Prior to the application of an input signal, the sampling fingers are precharged to the potential corresponding to a half-full CCD well by means of the biasing rail and gate shown on the left-hand side of Fig. IV-5. After the biasing gate is closed, a wideband signal is entered at the SAW transducer and generates a propagating surface wave with a piezoelectric displacement field. This field modulates the potential on each of the sampling fingers and thus modulates the charge in the storage wells in Fig. IV-5. This charge movement is sufficiently fast in a buried-channel device that it should be possible to use this technique for information bandwidths as high as 200 MHz. The sampling gate is shut in a time interval no longer than one-half an RF period, and a sampled replica of the SAW waveform is captured in the storage wells. With device leakage (dark) current of 1 nA/cm², a storage time as long as 1 sec can be obtained. When the transfer gate is opened and the storage gate closed, these captured charge packets are parallel-loaded into the CCD analog delay line and shifted out in a serial fashion at a rate determined by the CCD clock.

The full spatial content of the piezoelectric wave is not required. The required spacing of the sampling fingers can be determined by thinking in terms of an effective sampling frequency f_s , which is related to the spatial period of the sampling fingers S_c through the relation

$$S_c = V_s / f_s \quad (\text{IV-1})$$

where V_s is the velocity of the SAW. S_c is also the cell size of the CCD, since there must be one CCD cell for each sampling finger. The least count (minimum step) of our automated mask-making equipment dictates that S_c be a multiple of 2.54 μ m. Thus, f_s is limited to certain discrete frequencies. For the same reason, f_c (the input center frequency) is also limited to discrete values.

The effective sampling frequency f_s and the input center frequency f_c must be chosen carefully so that the output data stream is an accurate replica and does not lose any of the desired information from the input signal. In sampled data theory, such loss of information is called "aliasing," or frequency folding. What happens if f_s and f_c are not carefully chosen is shown in Figs. IV-6(a) and (c), where folding and spectral overlap can be seen.

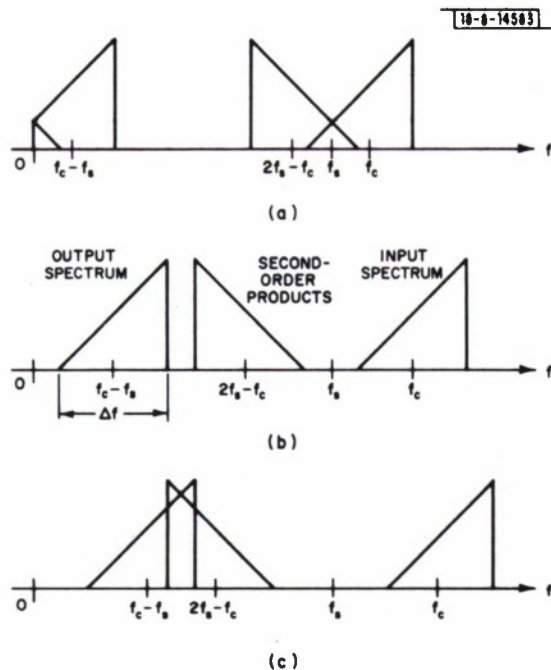


Fig. IV-6. Frequency spectrum of an input signal centered around f_c sampled at a frequency f_s : (a) f_c too low, (b) f_c acceptable, and (c) f_c too high. Frequencies above input frequency are not shown.

An appropriate procedure for selecting f_s and f_c is to choose a sampling frequency f_s high enough to prevent aliasing and which is compatible with the restrictions placed on the cell size S_c by the mask-making equipment. Given the specified signal bandwidth Δf and the sampling frequency f_s , there is a limited range of values of f_c which will not cause one of the problems depicted in Fig. IV-6. In the following paragraphs we will derive a set of inequalities which can be used to select f_s and f_c given Δf .

The effective sampling frequency is constrained to twice the desired information bandwidth by the sampling theorem:

$$f_s > 2\Delta f \quad . \quad (IV-2)$$

This relation can be used to select the effective sampling frequency. Once a sampling frequency has been chosen, there are limits on the permissible range of input frequencies. The input frequency f_{in} cannot be below the sampling frequency:

$$f_{in} > f_s$$

or if we let $f_{in} = f_c - \Delta f/2$ and rearrange:

$$f_c > f_s + \Delta f/2 \quad . \quad (IV-3)$$

There is also an upper limit on the input signal frequency. Second-order mixing products (sidebands of the second harmonic of the sampling frequency) must not overlap the output spectrum [see Fig. IV-6(c)]:

$$2f_s - f_{in} > f_{in} - f_s$$

or if we let f_{in} equal its maximum value of $f_c + \Delta f/2$ and rearrange:

$$f_c < (3f_s - \Delta f)/2 \quad . \quad (IV-4)$$

Inequalities (IV-3) and (IV-4) can be rearranged into one relation for the range of acceptable values for f_c :

$$f_s + \Delta f/2 < f_c < (3f_s - \Delta f)/2 \quad . \quad (IV-5)$$

The maximum value for the signal bandwidth permitted by relation (IV-5) is $\Delta f = f_s/2$, corresponding to a center frequency of

$$f_c = 5f_s/4 \quad . \quad (IV-6)$$

This frequency can be used as the target design frequency for the SAW input transducer.

When a center frequency has been chosen from one of the discrete values allowed, relations (IV-3) and (IV-4) can again be rearranged to find the resulting bandwidth. It is the smaller of the two values given by

$$\Delta f < \begin{cases} 2(f_c - f_s) \\ 3f_s - 2f_c \end{cases} \quad . \quad (IV-7)$$

Relations (IV-2), (IV-5), and (IV-6) can be used to select the effective sampling frequency and the center frequency when a certain bandwidth is desired. Relations (IV-7) and (IV-8) can then be used to find the maximum bandwidth resulting from the chosen values of f_c and f_s .

For our initial prototype, we wanted a bandwidth Δf of at least 25 MHz. If we use a lithium niobate SAW device ($V_s = 3430$ m/sec), relations (IV-1) and (IV-2) yield a maximum cell size of 68.6 μm . A cell size of 40.6 μm was chosen as more convenient from a mask-making point of view. This cell size corresponds to an effective sampling frequency f_s of 84.4 MHz, for which Eq. (IV-6) yields an optimum center frequency f_c of 105.5 MHz. 103.8 MHz is a convenient value, and relation (IV-7) tells us that such a choice will limit our bandwidth to 38.9 MHz, which is well above the desired value of 25 MHz.

Fabrication of the silicon CCD and the lithium niobate SAW delay line is complete. These components are being tested and will be assembled into a complete device in the near future.

D. L. Smythe

C. CHARGE-COUPLED DEVICES: IMAGERS

Fabrication of the 100- \times 400-element CCD imagers for the GEODSS (Ground Electro-Optical Deep Space Surveillance) program has been continuing. Recent yields based on static testing (gate-gate and gate-substrate shorts) have been encouragingly high, averaging about 14 percent for three runs of 6 wafers each, but dynamic test yields have been somewhat lower due to fabrication errors which have been corrected. Transfer inefficiency and dark-current levels have

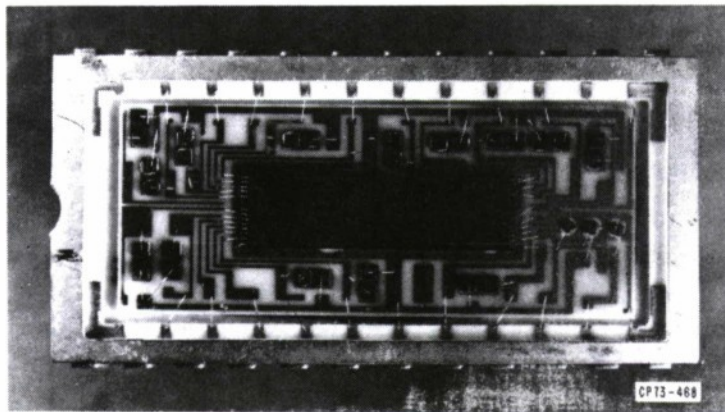


Fig. IV-7. Photograph of 100×400 CCD imager in 24-pin DIP. To provide protection against accidental static discharge, pairs of back-to-back Zener diodes are connected across device gates. In addition, an emitter-follower circuit is included in package to buffer output signal.

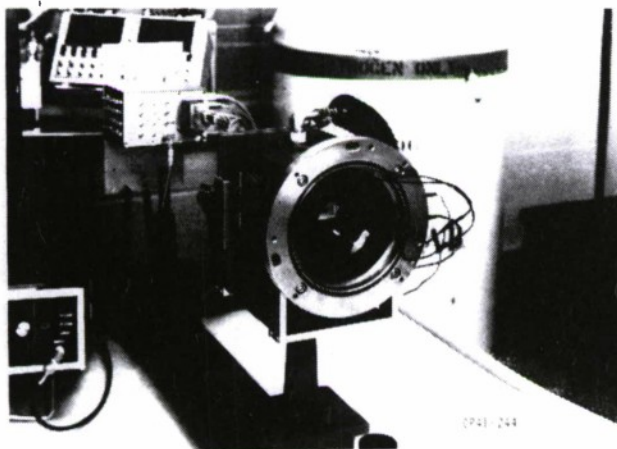


Fig. IV-8. Photograph of imaging CCD mounted in liquid N_2 -cooled Dewar with optical window.

improved considerably in the latest devices. Several chips have been packaged and are being tested as single-chip imagers operating in the "stare" mode. These devices will be evaluated on one of the telescopes at the GEODSS experimental test system² near Socorro, New Mexico.

Dynamic testing of these devices is done at the wafer level by means of a probe card which contains the driver circuits for clocking the CCD. The timing logic is generated separately and brought to the probe card by twisted pair leads. Locating the drivers on the probe card close to the device is done to minimize ringing and crosstalk resulting from the fast rise times of the pulses and is standard practice in commercial dynamic testing of integrated circuits. At present, all dynamic testing is performed with electrical input signals either to the output register alone or to the input register, in which case the entire 40,000-element array can be tested. In cases where the dark current is greater than about 100 nA/cm², the wafer must be cooled to permit testing. We have successfully probe tested devices at below -130°C by enclosing the prober in a plastic bag purged with dry N₂. Cold N₂ gas from a liquid source is circulated through the wafer chuck. It is not necessary for the interior of the bag to be completely moisture-free since the devices continue to function even after a thin layer of ice has condensed on the wafer.

Some processing problems have been revealed during dynamic tests, and corrective measures have been taken. One problem has been with the n⁺ diffusion along the input and output registers which serves as a charge drain to control blooming. Lateral diffusion of the phosphorous dopant had brought the n⁺ region too close to the signal channel in some devices, and this resulted in most or all of the signal charge being diverted into the blooming control drain. This problem was diagnosed in time to modify some of the processing times and temperatures on a partially completed device run. This procedure was partially successful, and, from the 6 wafers, 17 out of 24 devices which had passed static testing were successfully operated with electrical input signals.

Several chips from this recent run have been mounted in 24-pin dual in-line packages (DIPs) as shown in Fig. IV-7. Each gate on the CCD is protected from rupture due to electrostatic discharge by means of a pair of back-to-back 30-V Zener diodes. In addition, an emitter-follower circuit and the load resistor for the on-chip output MOSFET can be seen mounted in the package to the right of the CCD. The emitter follower provides signal buffering needed to drive the coaxial cable leading out of the Dewar in which the device is mounted (Fig. IV-8). Charge-transfer inefficiencies measured on the serial output register of these devices are about 2×10^{-5} per transfer, which is a considerable improvement over the value of 1.3×10^{-3} reported on an earlier device³ and is within the system specification of 8×10^{-5} . All such measurements are made with signals separated in time by at least 5 msec to ensure complete emptying of the mid-gap Au level. The improved transfer inefficiency indicates that we have successfully gettered or prevented the introduction of the high levels of Au contamination (see Sec. E below) which we had seen in earlier devices.³

Dark currents in the output register are correspondingly lower and are typically less than 4 nA/cm². However, many areas of the imaging portion of the devices have values in excess of 100 nA/cm². It is not presently understood why different regions of the same CCD have such widely differing dark currents.

A commercially available liquid N₂ Dewar[†] with an optical window has been obtained for a program of optical tests on individual imaging chips (Fig. IV-8). In the "stare" mode, the imager

[†] Products for Research, Model TE-251.

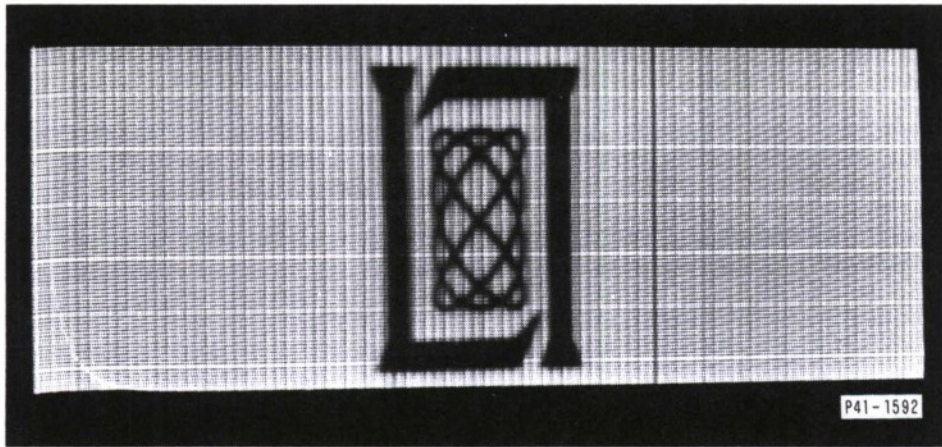


Fig.IV-9. Video monitor display of image projected onto 100- x 400-element CCD imager.

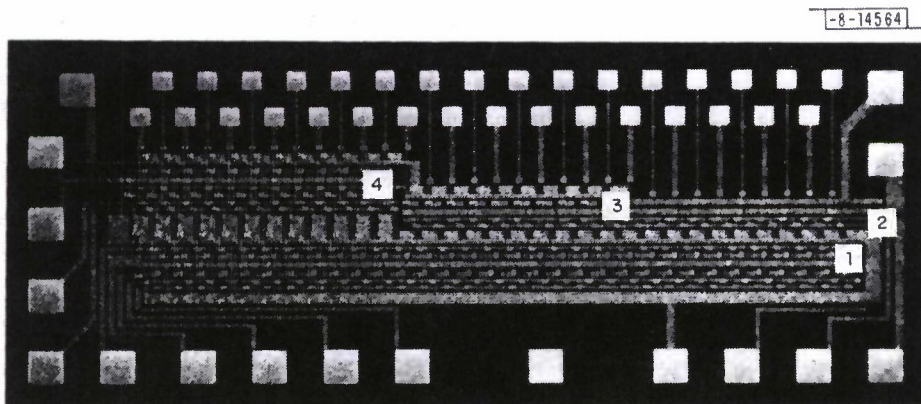


Fig.IV-10. Photograph of prototype n-channel MOS shift register showing (1) shift-register cells, (2) switches, (3) dynamic latches, and (4) static latches.

clocks are held stationary for an integration period, a shutter is then closed to shut off illumination of the device, and the signal charge is clocked out of the device. An example of the imaging quality is shown in Fig. IV-9. In this case, a transparency was focused onto a 100- × 400-cell device and the signal output was displayed on a TV monitor. Further tests of this imager in the stare mode are planned at the GEODSS test site.

B. E. Burke	R. W. Mountain
W. H. McGonagle	D. F. Kostishack
D. J. Silversmith	(Group 94)

D. CHARGE-COUPLED DEVICES: PROGRAMMABLE TRANSVERSAL FILTER

In previous reports,^{4,5} the structure of a high-speed CCD programmable transversal filter was described. The integration of MOS peripheral logic circuitry with the CCD structure required the development of a CCD-compatible MOS technology. During the past quarter, a test device consisting of an MOS shift register and latch circuits has been developed to demonstrate the feasibility of fabricating high-performance n-channel MOS logic devices using a process and substrate material which are also suitable for CCDs. The device is capable of operating at data rates from 0 to 8 MHz with an output amplitude from 0 to 10 V. Experiments have been performed to show that a digital reference can be stored in the static latch circuit while a new reference is being clocked in and out of the shift register.

A photomicrograph of the test device is shown in Fig. IV-10. For the final device, a static latch store is intended for use with the shift register. However, in this test device, a simple switch output and a dynamic latch are also included for evaluation purposes. The functions of each element shown in the photomicrograph are described below:

- (1) A digital reference function is serially loaded into the 32-stage, serial-in/parallel-out static shift register.
- (2) The output-enable switches separate the output nodes from the shift register.
- (3) A dynamic latch temporarily stores the reference function from the shift register.
- (4) A static latch holds the digital reference function indefinitely.

A shift-register cell consists of two ratio-inverter stages connected as a flip-flop by the clock lines. In operation, the source voltage V_{out} of the load FET in the inverter of Fig. IV-11 varies with respect to the fixed substrate bias. If the increase of threshold voltage versus the source-substrate bias is too fast (i.e., if the back-gate bias effect is too strong), V_{out} will not rise to the desired value or, in some cases, the circuit operation will be impaired. Furthermore, the zero-bias threshold voltage tends to be negative with the 1000-Å gate oxide thickness and high-resistivity substrate material which we intend to use for the CCD. Therefore, a boron-implanted channel region must be included to adjust the threshold voltage to the desired value without causing intolerable substrate bias sensitivity.

Based on a one-dimensional step-doping profile model,⁶ detailed analysis of an n-channel MOSFET device with an implanted channel region has been carried out in order to determine the acceptable channel implant dose and energy. The device design is shown in the inset of

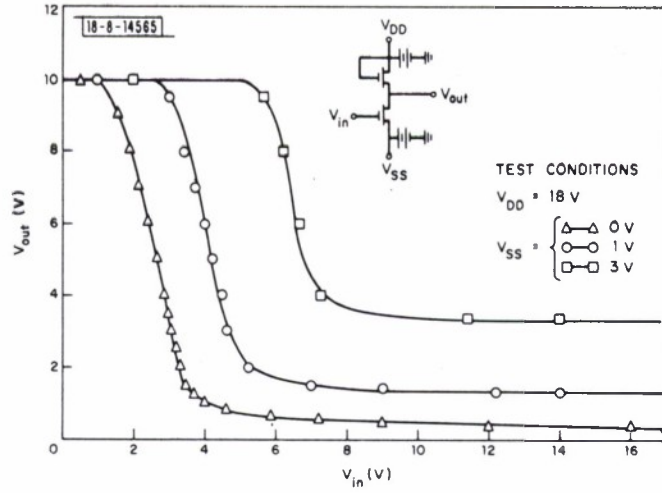


Fig. IV-11. Measured transfer characteristics for ratio inverter shown schematically in inset.

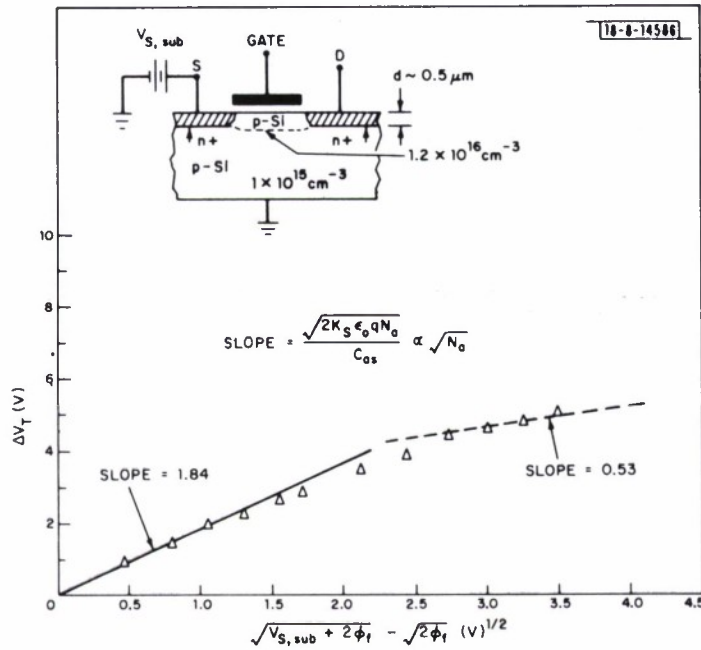


Fig. IV-12. Back-gate dependence of threshold voltage. Fermi energy level ϕ_f of 0.35 V was used in plot. Slopes were calculated using following parameters: $K_S = 11.7$, $C_{ox} = 3.43 \times 10^{-8}$ F/cm², $N_a = 1.2 \times 10^{16}$ cm⁻³ for initial slope, and $N_a = 10^{15}$ cm⁻³ for final slope. Symbols are defined in text.

Fig. IV-12. Boron implant was used to raise the substrate doping in the region under the gate. Based on the above-mentioned model, the dependences of threshold voltage on source-substrate bias are as follows.

When $W \leq D$,

$$V_T = V_{FB} + 2\phi_f + \frac{\sqrt{2K_S\epsilon_o q N_{a,S}}}{C_{ox}} \sqrt{V_{S,sub} + 2\phi_f} \quad (IV-9)$$

where W is the depletion-layer depth under the gate, D is the boron-implanted depths after drive in, V_{FB} is the flat band voltage, ϕ_f is the Fermi potential of the substrate, K_S is the dielectric constant of silicon, ϵ_o is the free-space permittivity, q is the electron charge, and $N_{a,S}$ is the doping concentration of the implanted surface region.

When $W > D$,

$$V_T \cong V_{FB} + 2\phi_f + \frac{q(N_{a,S} - N_{a,B}) D}{C_{ox}} + \sqrt{\frac{2qN_{a,B}}{K_S\epsilon_o(V_{S,sub} + 2\phi_f)}} \times \left[\frac{q(N_{a,S} - N_{a,B}) D^2}{4C_{ox}} \right] + \frac{\sqrt{2K_S\epsilon_o q N_{a,B}}}{C_{ox}} \times \sqrt{V_{S,sub} + 2\phi_f} \quad (IV-10)$$

where $N_{a,B}$ is the "unimplanted" bulk substrate doping concentration. Equations (IV-9) and (IV-10) indicate two important consequences. First, by using ion implantation to raise the surface doping concentration under the gate, the zero-bias threshold voltage of a high-resistivity substrate n-channel MOS can be adjusted to the desired positive value. Second, when the depletion-layer depth under the gate is greater than the boron-implanted depth, the dependence of the threshold voltage on the source-substrate bias (or the slope of V_T vs $\sqrt{V_{S,sub} + 2\phi_f}$) is determined by the impurity concentration of the unimplanted bulk substrate, not by the implanted layer. The results of this analysis were used to specify that the channel implant dose for these wafers was $5 \times 10^{11} \text{ cm}^{-2}$ at an energy of 70 keV. The measured threshold voltage as a function of source-substrate bias for a typical device is shown in Fig. IV-12. It shows different regions of dependence of threshold voltage on the source-substrate bias, i.e., the initial dependence on the surface doping and the final dependence of the bulk doping. The net result is that as $V_{S,sub}$ increases from 0 to 18 V, the increase in threshold voltage is only from 1.3 to 6.3 V. This result clearly demonstrates that the back-gate bias effect can be controlled with an appropriate channel implant.

Care must also be given in determining the boron implant depth when these n-channel MOSFETs are to be used as the switching devices shown in Fig. IV-10. The implanted p-type region not only has to give the desired threshold dependences, but also has to control the extent of the source and drain depletion regions. With the gate turned off, these depletion regions must be kept separated. As shown in the inset of Fig. IV-12, the selected boron implant together with implanted source and drain helps to increase the source-drain punch-through voltage of a high-resistivity substrate material.⁷

The performance of the shift register and latch circuits has been measured. The shift register can be operated from 0 to 8 MHz, and the performance of the shift register operating at 8 MHz is shown in Fig. IV-13. The device also has been operated at rates as slow as 666 Hz, and the input signal has been delayed for about 4.8 msec after clocking through the shift register.

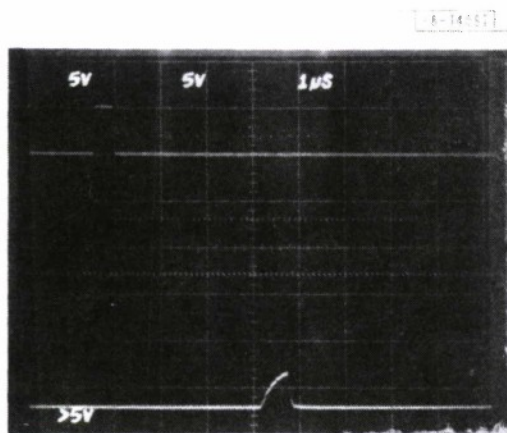


Fig. IV-13. Performance of shift register shown in Fig. IV-10. Upper trace is clock waveform, bottom trace is output from shift register. Clock frequency is 8 MHz, and signal delay is 3.8 μ sec.

Since the test device is intended to be used as a static shift register, an experiment has been performed to show that information can be stored in the shift register indefinitely as long as the clocks are stopped in the appropriate states and the power is on. The capability of the device to store a digital reference in the static latch circuits while a new reference is being loaded into the shift register has also been established. As long as the transfer switch is opened and the feedback loop is closed, the data are permanently stored in the flip-flops.

In all these tests, the high state output of the device is about 10 V when V_{DD} is biased at 18 V; the low state output is about equal to V_{SS} , which can vary from 0 to 5 V. These results are also confirmed by the measured transfer characteristics of a single-stage inverter, shown in Fig. IV-11. These test data indicate that a comfortable operating range can be provided by the n-channel MOS logic circuit for controlling the input diodes of the CCD delay lines.

A. M. Chiang R. W. Mountain
B. E. Burke D. J. Silversmith
D. L. Smythe

E. WAFER-PROCESSING TECHNIQUES FOR MINIMUM DARK CURRENT

Dark current in buried-channel, charge-coupled devices results from recombination centers (traps) whose energies lie within the silicon band gap. These traps are usually associated with heavy metal contaminants, particularly gold.³ An initial heavy phosphorous diffusion on the wafer back side getters heavy metal contaminants in as-received silicon wafers, and this doped layer will continue to getter heavy metals introduced from the subsequent processing environment as long as it is in place. Dark-current levels J_D of 1 nA/cm² have been achieved on gate-controlled diodes using this process.

A dark current of 10 nA/cm² (which is the required level for the large-area imaging CCDs) corresponds to a carrier lifetime t_0 of approximately 120 μ sec. The corresponding gold-trap density is given by

$$N_t = \frac{1}{\sigma_n V_{th} t_0} = 2 \times 10^{11} \text{ cm}^{-3}$$

where σ_n (the capture cross section) is $4 \times 10^{-15} \text{ cm}^2$, and V_{th} (the thermal velocity) is 10^7 cm/sec (Ref. 8). An additional dark-current source is the mid-gap fast-interface states. However, with proper annealing the interface state density can be kept low, and in our devices their contribution to the dark current is less than 1 nA/cm².

Proper wafer-processing techniques can reduce N_t to $2 \times 10^{11} \text{ cm}^{-3}$ or less, significantly below the levels which would be otherwise expected. Measurements of gold levels in unprocessed wafers⁹ are in the range 10^{11} to 10^{14} cm^{-3} . In addition, gold introduced from acid etches can result in surface concentrations of 10^{12} to 10^{13} cm^{-2} on silicon wafers; this leads to $N_t = 10^{14} \text{ cm}^{-3}$ when the wafers undergo high-temperature heat treatment,¹⁰ although the wafer-cleaning process in current use reduces this value to no more than 10^{13} cm^{-3} (Ref. 11).

Using the gettering effect of a high-concentration ($>10^{19} \text{ cm}^{-3}$) phosphorous diffusion along with the protection of an oxide layer has been shown to reduce gold traps to an acceptable level,¹² and these modifications have been incorporated into our processing schedule. In order to create a suitable gettering layer, phosphorus is diffused into wafer backs and serves a dual purpose. Not only is gold gettered, but crystalline defects in the as-received wafers are gettered as well. This so-called POGO (pre-oxidation gettering of the other side) process^{13,14} uses a POCl_3 source in a 1150°C furnace for 4 hr. Gate-controlled diodes¹⁵ fabricated with this back-side diffusion had $N_t < 2 \times 10^{10} \text{ cm}^{-3}$ or $J_D < 1 \text{ nA/cm}^2$. Tests have also shown that the N^+ POGO layer is effective in gettering gold contamination due to etches and atmospheric impurities.

An experiment was undertaken to study the effects of this phosphorous-doped layer through the processing sequence. Twelve 40-ohm-cm (100) float zone grown wafers were separated into two six-wafer lots after POGO treatment. Six wafers followed a previous process that removes the POGO diffused layer by a 20- μm back-side etch prior to oxidation. On the other six wafers, the POGO layer was left intact. Subsequent processing involves the formation of an 800- \AA SiO_2 and 1500- \AA Si_3N_4 gate dielectric, a 15-min. phosphorous diode diffusion, and 1000°C N_2 anneals for various periods of 20 min. to 6 hr with back-side oxide removed. All wafers were then annealed at 900°C in H_2 for 15 min. and metallized with aluminum to form gate-controlled diode structures. Wafers which had been stripped of their POGO layer before initial oxidation suffered dark-current increases in proportion to their subsequent N_2 anneal times (from $<5 \text{ nA/cm}^2$ to 1 mA/cm^2). In contrast, wafers with the POGO layers left on during subsequent processing show $J_D < 5 \text{ nA/cm}^2$ regardless of anneal times. The six-orders-of-magnitude increase in N_t for the stripped POGO wafers cannot be explained by gold plating from etchants alone. This enormous increase may be evidence of impurities introduced from other sources in the processing environment.

When retaining the POGO layer, one must be careful that hot processing does not reduce the N^+ concentration by outdiffusion or deeper diffusion to the point where the phosphorus no longer getters.¹⁶ Our tests indicate that this does not occur in our present processing scheme.

D. J. Silversmith	D. M. Smith
R. W. Mountain	B. E. Burke

REFERENCES

1. E. Sauter and G. V. Schultz, IEEE Trans. Microwave Theory Tech. MTT-25, 458 (1977); and H. Kräutle, E. Sauter, and G. V. Schultz, "Antenna Characteristics of Whisker Diodes Used as Submillimeter Receivers," Radio Astronomy Research Report No. 131, Max-Planck-Institut für Radioastronomie, 53 Bonn, Germany (1977).
2. "GEODSS Experimental Test System Summary Report - FY 1975," Project Report ETS-1, Lincoln Laboratory, M.I.T. (12 January 1976), DDC AD-B009987-L.
3. Solid State Research Report, Lincoln Laboratory, M.I.T. (1977:1), p. 31, DDC AD-A041226/2.
4. Ibid. (1976:4), pp. 56-61, DDC AD-A039175.
5. Ibid. (1977:1), pp. 29-31.
6. V. L. Rideout et al., "Device Design Consideration for Ion Implanted MOSFETs," IEDM Digest, 1973, pp. 148-151.
7. R. H. Dennard et al., "Ion Implanted MOSFETs with Very Short Channel Lengths," IEDM Digest, 1973, pp. 152-155.
8. R. O. Carlson, J. Appl. Phys. 29, 1001 (1958).
9. S. P. Murarka, J. Electrochem. Soc. 123, 765 (1976).
10. G. Bemski and J. D. Struthers, J. Electrochem. Soc. 105, 588 (1958).
11. W. Kern and D. A. Puotinen, RCA Review 31, 187 (1970).
12. T. A. O'Shaughnessy, H. D. Barber, D. A. Thompson, and E. L. Heasell, J. Electrochem. Soc. 121, 1350 (1974).
13. G. A. Rozgonyi, P. M. Petroff, and M. H. Read, J. Electrochem. Soc. 122, 1725 (1975).
14. G. A. Rozgonyi and R. A. Kushner, J. Electrochem. Soc. 123, 570 (1976).
15. A. S. Grove, Physics and Technology of Semiconductor Devices (Wiley, New York, 1967), p. 296.
16. H. Higuchi and S. Nakamura, Abstract 175, The Electrochemical Society Extended Abstracts, Spring Meeting, May 1975, p. 412.

V. SURFACE-WAVE TECHNOLOGY

A. PRECISION SAW FOURIER-TRANSFORM SYSTEM

The precise linear-FM response which can be obtained from reflective-array compressors (RACs) has made possible the realization of large-bandwidth Fourier-transform systems that use surface-wave devices. Such systems offer the potential advantages of high speed combined with smaller size and less power consumption than equivalent digital systems. A 300-point Fourier-transform system with a bandwidth of 10 MHz has been breadboarded for the first phase of the demonstration of the performance of this analog approach. The system is designed for a combination of high precision and wide dynamic range in the Fourier transform.

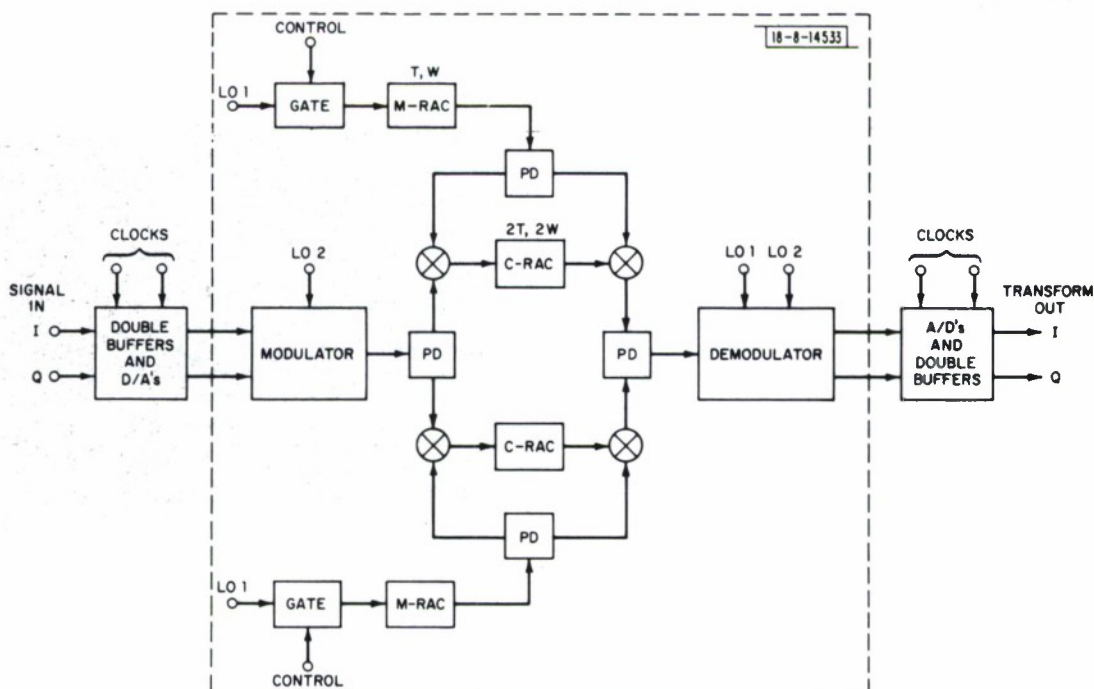


Fig. V-1. Hybrid chirp-Fourier-transform system in which input and output are digital data.

The complete system which is under construction is illustrated in block form in Fig. V-1. The system can operate asynchronously with contiguous blocks of data, each block consisting of 256 words, at an input rate up to 10 MW/sec in both I and Q channels. The data are read into buffer memories at a rate determined by the data source. After the input registers are full, the data are read out through the D/A converters under control of the system internal clock. Meanwhile, the next block of data is being loaded into the memories. The modulator serves to shift the data now converted to an analog signal, to a convenient IF, after which the signal is routed to two chirp-transform systems. The two transform systems operate in a "ping-pong" mode. The analog portion of the chirp-transform system could easily be designed to operate

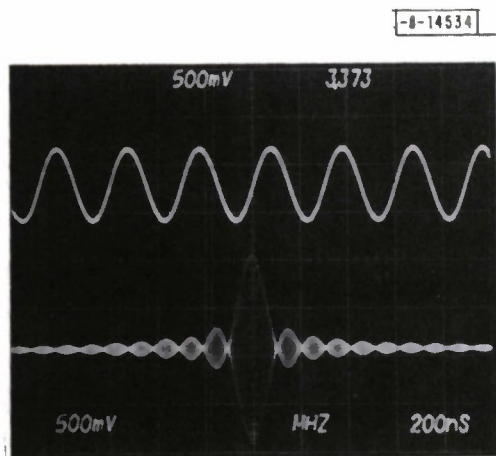


Fig.V-2. Chirp Fourier transform of sine wave. Upper trace: input sine wave; lower trace: Fourier transform.

Fig.V-3. Chirp Fourier transform of square wave. Upper trace: input square wave; lower trace: Fourier transform.

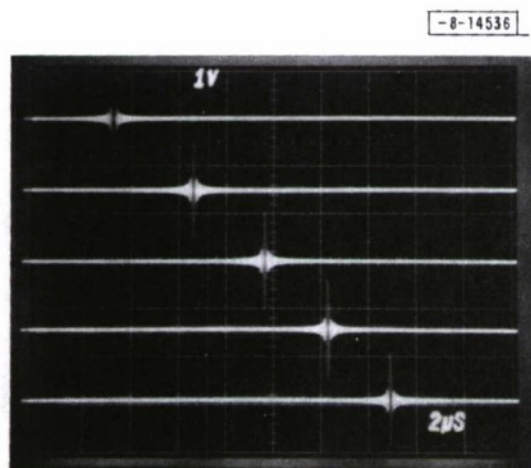
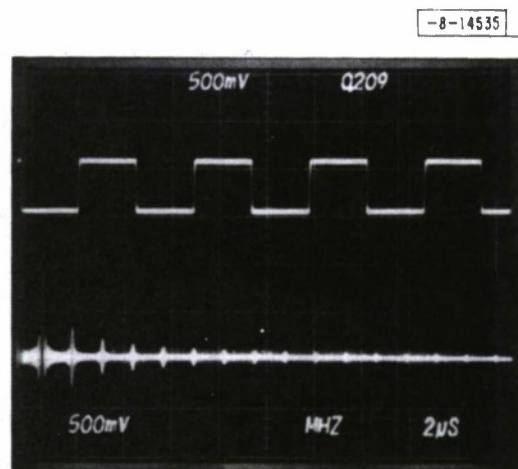


Fig.V-4. Chirp Fourier transform of input sine waves at 1, 2, 3, 4, and 5 MHz, respectively, starting at upper trace.

at much higher bandwidth (>20 MHz) and thus accommodate a net throughput rate of 10 MW/sec by operating at less than 50-percent duty factor. In principle, this would remove the need for operating in the ping-pong mode. However, this mode was chosen because the lower bandwidth places less severe restrictions on the D/A's and A/D's.

The ping-pong chirp-transform system requires four RAC devices, two used for pre- and post-multiplication (M-RACs), and two used for convolution (C-RACs). Since the system bandwidth is the difference between the bandwidth of the convolution device and that of the multiply chirp, maximum system time-bandwidth is achieved if the convolution device has twice the bandwidth and dispersion of the multiply chirp. Since lower insertion loss of the RAC devices is achieved if they have a downchirp impulse response, all the RACs are so constructed. Therefore, the lower sideband signal is chosen after the first mixer in order to invert the chirp and match the C-RAC filter. The lower sideband is also required after the second mixer in order to remove the quadratic phase characteristic from the now Fourier-transformed signal. The demodulator serves to convert the transformed signal to baseband I and Q signals. Finally, the transformed signals are converted to digital and read out through buffer memories similar to those at the system front end.

The section of the system which is inside the dashed box in Fig. V-1 has been breadboarded using RAC filters originally designed for another program. The parameters of this breadboard system are listed below.

Breadboard System Parameters

	Center Frequency (MHz)	Bandwidth (MHz)	Dispersion (μsec)	CW Insertion Loss (dB)
M-RAC	70	10	30	22
C-RAC	95	20	60	30
LO 1	70	—	—	—
LO 2	165	—	—	—

The performance obtained with some representative waveforms is shown in Figs. V-2 through V-4. Figure V-2 shows the transform of a CW waveform and illustrates the high signal-to-noise ratio (SNR) and lack of distortion of the system. Since the system effectively gates the input waveform to the time duration of the multiplying chirp, the transform is that of a 30-μsec gated RF pulse, i.e., a $(\sin x)/x$ function. Although the system was not optimized, it was possible to attenuate the CW input by more than 70 dB and still detect an output above noise, thus indicating a large dynamic range. Actually, the amplitude of the output is a function of the nature of the input signal. For example, maximum output signal is achieved with a CW input, whereas, if the input were a video pulse, the output would be lower by the ratio of the video pulse length to the length of the transform, i.e., to the dispersion of the pre-multiplying chirp.

Figure V-3 illustrates the Fourier transform of a square-wave input showing all odd harmonics falling off as $(n)^{-1}$. Figure V-4 illustrates the Fourier transform of a series of input CW waveforms from 1 to 5 MHz. The signals were inserted only into the I channel. Therefore, both sidebands were generated in the modulator, and an equivalent series of lower sidebands could be seen (but not shown) symmetric about the zero-frequency point. This illustrates the system bandwidth of 10 MHz.

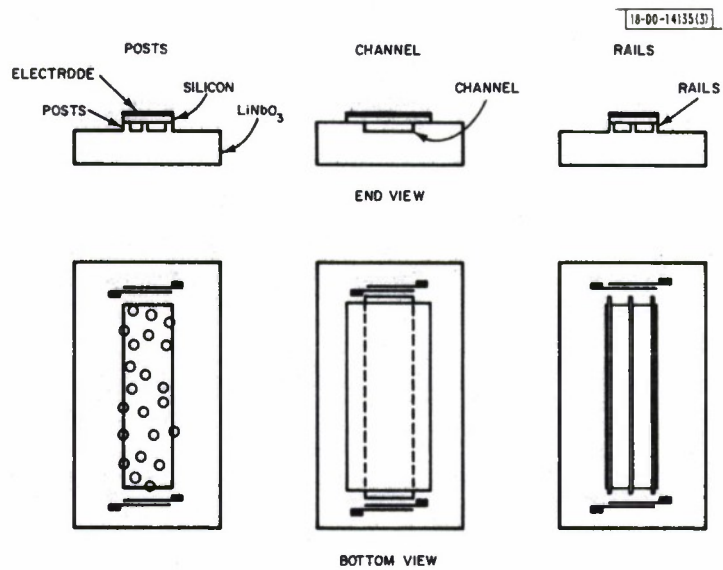


Fig.V-5. Post, channel, and rail support structures employed in gap-coupled acoustoelectric SAW devices.

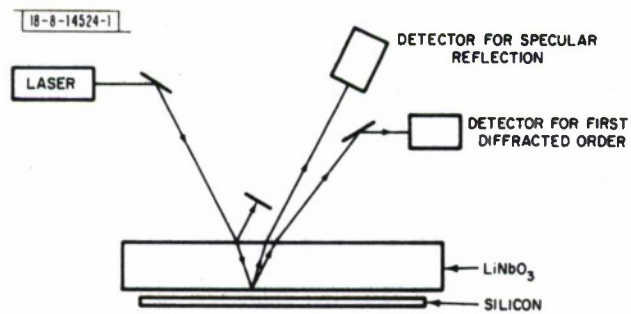


Fig.V-6. Laser probe for measuring beam profiles in acoustoelectric convolvers.

In the second phase of the SAW Fourier-transform program, an improved brassboard version of the complete system will be constructed. New RAC devices have been designed to operate at center frequencies which have been chosen to avoid all mixer intermodulation spurious up to seventh order. The buffer memories and timing-control circuitry are being designed to allow interfacing with the IBM 370 computer for system exercise and evaluation. In addition, the amplifiers and other RF components have been chosen to maximize output SNR. The D/A's and A/D's are each to have at least 8-bit accuracy at 10 MW/sec digital rate. This system will provide the desired combination of accuracy, speed, and dynamic range and will allow direct comparison with competitive digital processors.

M. B. Schulz

B. PROPAGATION MODES IN GAP-COUPLED ACOUSTOELECTRIC DEVICES

The acoustoelectric convolver developed at Lincoln Laboratory is a composite structure consisting of a LiNbO_3 delay line and a silicon strip separated from the delay line by an intervening air gap.¹ A series of posts (or rails) ion beam etched into the LiNbO_3 surface maintains a stable air gap over a wide temperature range.² This structure has been used in several types of acoustoelectric devices. Optical-probing data of SAW propagation under the silicon have demonstrated that the silicon in place over the delay line weakly guides the surface wave and forms an overmoded waveguide. The support structure (posts or rails) modifies the mode pattern and can cause intermode coupling or scattering out of the waveguide, thus degrading the device performance.

The effects of the support structure have been investigated theoretically³ and experimentally, and improved supports have been identified. Three basic types of silicon support structures – posts, rails, and a channel – have been fabricated on LiNbO_3 delay lines, as shown in Fig. V-5. With these structures, it was possible to compare the delay-line loss with and without the silicon in place. The magnitude of the acoustoelectric attenuation of the surface wave due to the presence of the resistive silicon can be predicted theoretically. The remainder of the added loss, termed excess loss, is due to moding effects and scattering of the surface waves by the support structure into bulk and other surface waves.

An optical probe was set up for monitoring the profile of the acoustic beam as it propagates under the silicon.⁴ A He-Ar laser beam is directed through the back side of the LiNbO_3 delay line as shown in Fig. V-6. The surface wave diffracts a fraction of the beam energy. Two PIN-diode detectors are set up to intercept the reflected laser radiation. One measures the specular reflection from the surface of the LiNbO_3 which carries the surface wave (front surface), and the second detector measures the energy which has been diffracted by the surface wave into the first-order Bragg angle. The ratio of the detector output is approximately proportional to the power of the surface wave. The ratio measurement nearly compensates for variations of reflection and transmission in LiNbO_3 and for the effects of multiple reflections which occur between the LiNbO_3 and the silicon.

Measurements were made of SAW propagation under a silicon strip supported by a random array of posts which were 5 μm in diameter and were located on 4- \times 8-mil centers with ± 2 -mil randomization. The profile of the SAW varied considerably from device-to-device even under the most controlled fabrication procedures. In some cases the acoustic beam profile was fairly uniform down the length of the silicon strip, and the excess loss was as low as 2 dB. In other

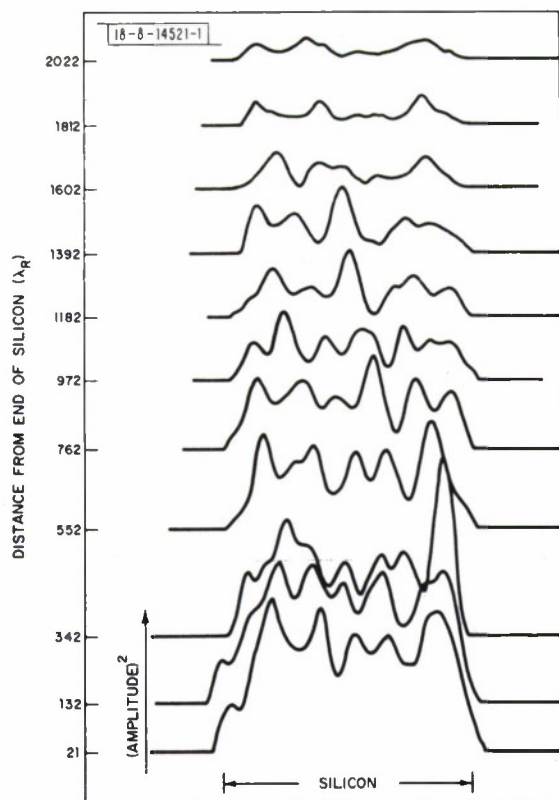
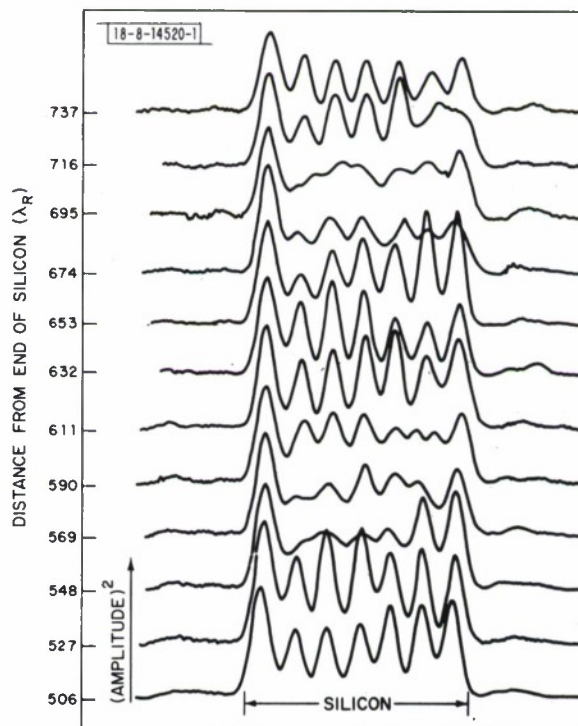


Fig.V-7. Beam profiles for surface wave propagating under silicon strip with post support structure.

Fig.V-8. Beam profiles for surface wave propagating under silicon strip with support structure consisting of 8 parallel rails.

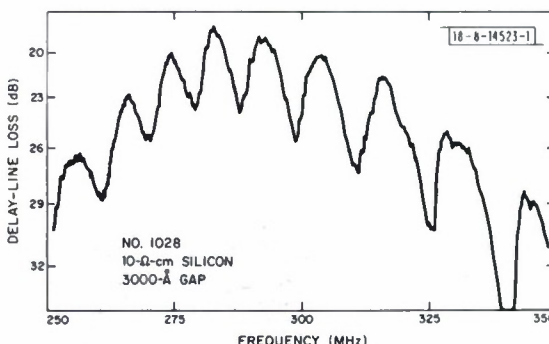


cases, the beam profile varied considerably, as shown in Fig. V-7, and the excess loss was 8 dB or more.

The profile of the acoustic wave propagating under a silicon strip with a channel-type support was also measured. The width of the channel was 60 mils and the exciting transducers had an aperture of 30 mils. The device had a nominal gap spacing of about 4500 \AA . The spring pressure holding the silicon in place bowed the silicon toward the delay line by about 800 \AA . This bowing tended to concentrate the acoustic energy toward the center of the silicon strip as it propagated under the silicon. This structure had a minimum amount of excess loss, 2 to 3 dB, in comparison with other support structures. Unfortunately, this structure is not stable with respect to variations in temperature and could not be used for our final design.

Joly⁵ reported low losses when using a support structure consisting of equally spaced narrow rails, but with shorter lengths (2 cm) of silicon than commonly used in the Lincoln Laboratory devices (3.5 to 7 cm). Our first rail devices were fabricated with $6.5\text{-}\mu\text{m}$ -wide rails on $100\text{-}\mu\text{m}$ centers. These showed considerable amounts of excess loss, namely, 5 to 6 dB. In addition, the rail devices showed a "beating" phenomenon between the fundamental and a higher-order mode as shown in Fig. V-8. The two modes had characteristic beat lengths of $137\lambda_R$ at 300 MHz, where λ_R is the wavelength of the surface wave. The beating phenomenon also showed up in the frequency response of the delay line, as shown in Fig. V-9. Beat lengths close to this value were predicted analytically by Wang.³

Fig. V-9. Frequency response of delay line with 8-rail support structure. Ripples due to beating between modes is evident.



The support structure which is currently yielding the best results consists of three $4\text{-}\mu\text{m}$ -wide rails on 14.5-mil centers. The three rails provide the minimum amount of support which will still ensure temperature stability. Analysis by Wang³ indicated the desirability of reducing the rail width. While the rail width was reduced from 6 to $4\text{ }\mu\text{m}$ in the current design, a rail width of only $2\text{ }\mu\text{m}$ would still provide about twice the support area of the post structure. Experimental data on post and channel support structures indicated a tendency for a null in the beam profile to form at the center of the silicon strip. Using this clue, we placed one rail at the center and an additional rail near each side of the silicon strip.

The acoustic profile under the silicon for a $20\text{-}\mu\text{sec}$ device with a three-rail support structure is shown in Fig. V-10. Here we see the emergence of a 2-lobe beam profile which remains relatively stable under the entire 7-cm length of the silicon. Insertion-loss measurements indicate an excess loss of only 2 dB. The frequency response of this device shows no substantial interference between different modes in the structure.

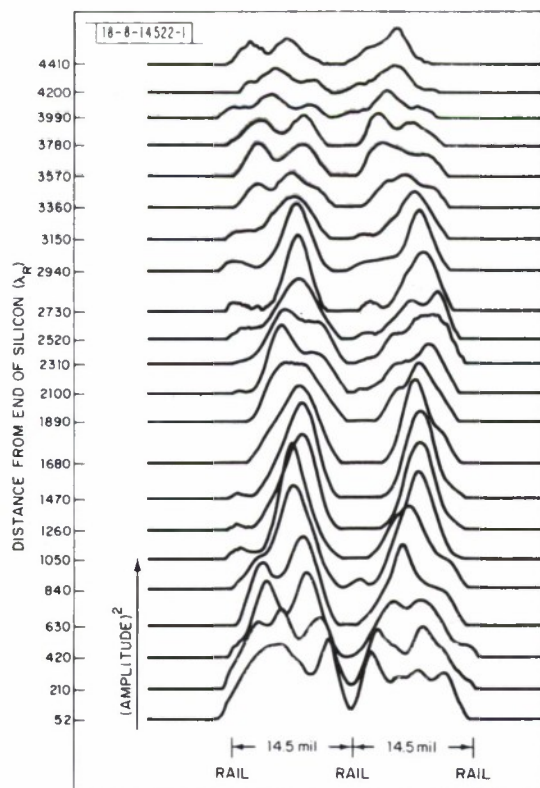


Fig.V-10. Beam profiles for surface wave propagating under silicon strip with support structure consisting of 3 parallel rails.

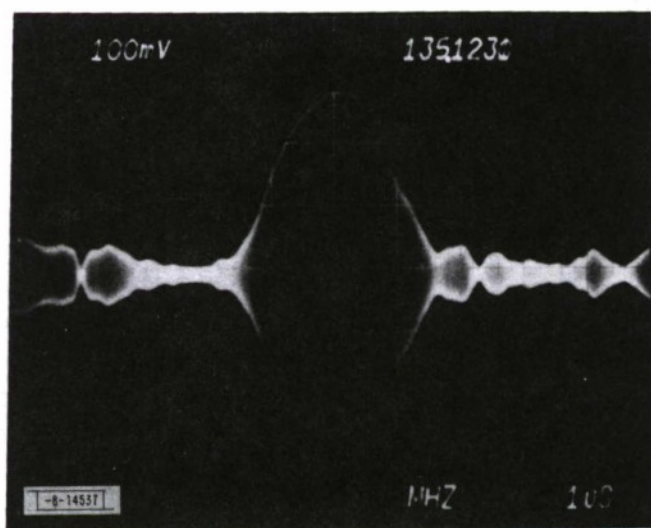


Fig.V-11. Typical output correlation peak from an integrating correlator.

Using the three-rail support structure and several other improvements has increased the conversion efficiency of the DPSK convolvers from a previously reported value² of -82 dBm to efficiencies of -77 dBm. Equally important is the observation that the convolvers have much more repeatable characteristics.

S. A. Reible
V. S. Dolat
J. H. Cafarella

C. ACOUSTOELECTRIC INTEGRATING CORRELATOR

The device structure and operating principle of the acoustoelectric integrating correlator were described in a previous report.⁶ By utilizing the slow charging of a diode array by counter-propagating SAWs, this device can correlate phase-coded waveforms which are several orders of magnitude longer than the transit time of the acoustoelectric interaction region.

A typical output from a device with a transit time of 10 μ sec is shown in Fig. V-11. This 135-MHz output was obtained when both signal and reference were 21-dBm, 67.5-MHz, pseudo-noise biphasic waveforms modulated at a 250-MHz chip rate and integrated over a 10-msec code segment. The read waveform at 136 MHz was a 2- μ sec-long 25-dBm pulse. The output level is -42 dBm.

The major spurious signal level in this first-generation device is associated with the read waveform, as can be seen in Fig. V-12. No signal or reference was entered here, just the 25-dBm read waveform. It appears that bulk acoustic waves are being launched by the transducer and are being detected by the silicon output circuit. Future devices will incorporate means of quenching these bulk modes.

A critical requirement for the integrating correlator is that the integration be sensibly linear in time, for only then can full signal-processing potential be realized. The data which follow demonstrate such linearity, and, in fact, were obtained by operating the device in a typical

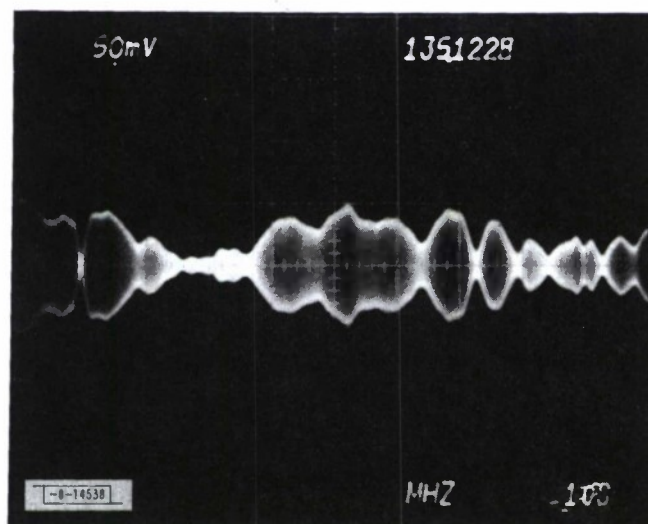


Fig. V-12. Output obtained under same conditions as Fig. V-11 except that no signal has been entered. Spurious signal level shown is generated by read pulse.

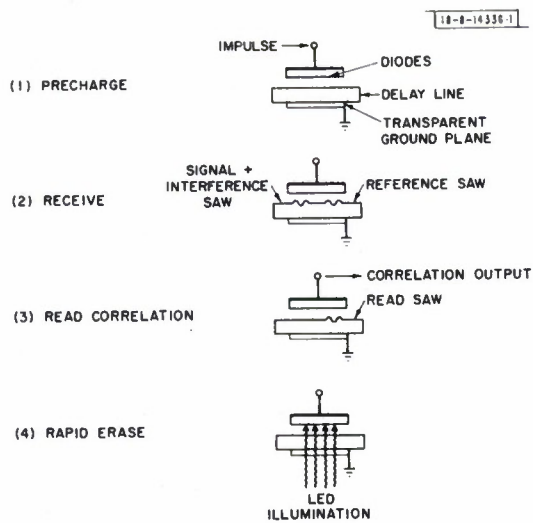


Fig.V-13. Sequence for linear operation of integrating correlator.

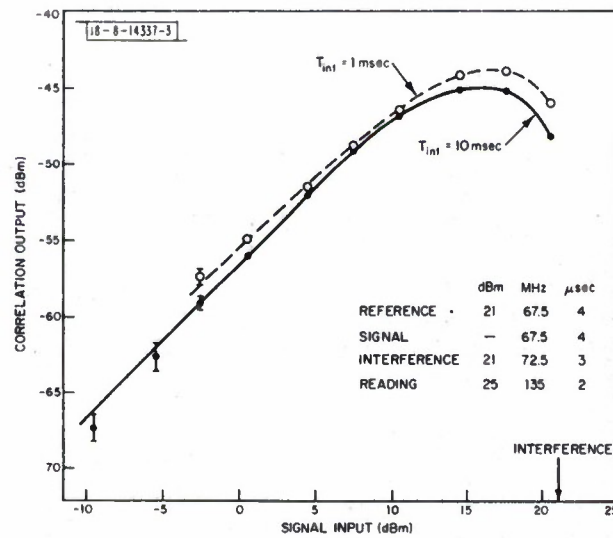


Fig.V-14. Linearity of output vs input for weak signal plus strong interference correlated with strong reference.

spread-spectrum-communications mode, i.e., with an incoming waveform consisting of the desired signal plus interference in the form of a high-level pseudonoise waveform. This test was constructed to simulate an applications area of interest. Specifically, the device was operated in the sequence shown in Fig.V-13. A 250-V, 5-nsec impulse is applied through the output port to precharge the diode array into uniform reverse bias. This self-reverse bias stays essentially fixed through the receive and read modes. The reason for the bias is to ensure that the propagation conditions are constant for all segments of the long signal and reference waveforms. In the absence of a precharge, the first segment of the input waveform would see a smaller depletion depth, which results in a slowing of the wave and accompanying dephasing relative to later code segments. Dephasing due to velocity variations is more fully discussed elsewhere.⁷ The receive mode commences 400 μ sec after the precharge, and the readout occurs 100 μ sec after the integration is completed. Because of the long storage time of the array, green LEDs are used to erase the array at the end of the cycle.⁷ This allows fast recycle time without cycle-to-cycle effects.⁸

Figure V-14 indicates the linearity of signal output to signal input for integration times of 1 and 10 msec. The chip rate for signal and reference was 250 kHz, the free-running clock for the pseudonoise interference was at 330 kHz. Because of the high spurious levels generated by the read waveform in this device, a cancellation scheme had to be employed to reduce this spurious level in order to obtain the low-power data. Significantly, the device is linear for ratios of interference power to signal power less than 10. The linearity is good for both integration times, implying that the signal-processing gain should approach the (bandwidth) \times (integration time) products of 24 and 34 dB for the two cases plotted. Not indicated in the figure is the fact that, for the shorter integration time, the interference level at the output was approximately 10 dB higher than for the longer integration time, a result which is consistent with the difference in signal processing. Initial tests of the integrating correlator's response to a weak signal dominated by white noise show similar results, i.e., a high noise-rejection capability.

If one defines a figure of merit as the ratio of output power to input powers, then for an untuned output port under the optimum condition where the device is filled with a uniform-amplitude correlation waveform and the readout pulse fills the interaction region, the three-wave interaction within the device has a -86-dBm^2 efficiency. As expected, the three-wave interaction is less efficient than the more typical two-wave interaction used in convolvers.²

Another aspect of the device linearity is shown in Fig.V-15. In this case the signal was gated on for only 1/5 of the full integration time, and its position within the full integration interval was scanned. The reference and interference remained on throughout the full integration time. The output for each segment is normalized to the full integration output. A true linear integrator would give equal weight to each segment, with the output down 14 dB. Segmenting the 1-msec integration indicates nearly equal weights, but about 2-dB-higher value than ideal. The 10-msec integration, whether read 0.1 or 10 msec after integration, tends to weight the later segments too much. The probable cause is the relaxation of the precharge bias and the stronger interaction of the silicon with the counterpropagating waves.

The mechanism by which reasonably linear charge integration is obtained over long time sequences is as follows. Hard forward bias of the diodes must be avoided, since in that case the diode array charges logarithmically, as would be expected of a distributed peak-detector circuit.⁸ Instead, an initial uniform reverse bias is set by the precharge impulse, and is essentially maintained at that level throughout the long integration time by the strong counterpropagating references and interference inputs. Thus, throughout the receive sequence, the weak

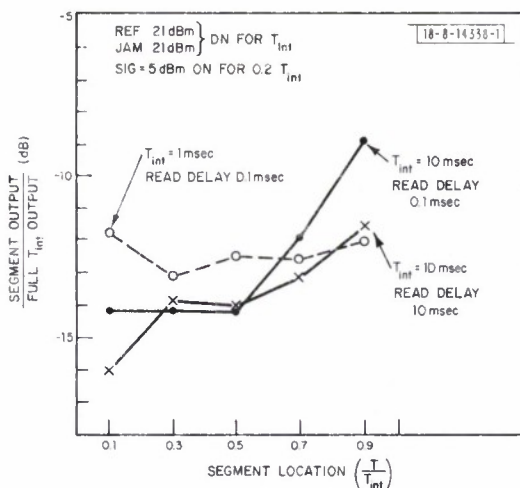


Fig. V-15. Weights of various segments of long code when processed by integrating correlator.

quasi-static potential produced by the counterpropagating reference and signal inputs is linearly integrated by the reverse-biased diodes. In the limit of high signal power (>10 dBm) or time approaching the storage time (~ 30 msec), the integration deviates substantially from the desired linear characteristic.

The realization of the full processing gain of a large-bandwidth code awaits a device modification. This is required to avoid excessive filling-factor loss and to maintain dynamic range. Filling-factor loss affects the output power; this is due to the electrical loading of the active length by the passive length during the readout process. The active length can be very short because the correlation peak is very narrow when a wideband signal is integrated. For example, reference and signal codes of 20-MHz bandwidth would result in a triangular correlation waveform being stored in the structure with a half-width of 9×10^{-3} cm. Thus, a device with a 3.5-cm interaction length (20- μ sec time window) would have an unacceptable filling-factor loss of 52 dB. The proposed solution is to spatially spread the integrated signal and read it with an expanded read pulse by using phase-coded transducers for the reference and read waveforms and a standard transducer for the signal. This should produce a narrow compressed pulse with low sidelobes, and would read out the correlation peak with a filling-factor loss of only about 10 dB.

Present efforts are being directed toward the realization of an optimum device structure with low spurious levels and small filling-factor loss for the processing of 20-MHz-bandwidth codes of up to 10-msec duration with wide dynamic range, and a potential signal-to-noise enhancement of 54 dB.

R.W. Ralston	J.H. Cafarella
D.H. Hurlburt	E. Stern
F.J. Leonberger	

REFERENCES

1. Solid State Research Report, Lincoln Laboratory, M.I.T. (1976:3), p. 57, DDC AD-A027261.
2. S. A. Reible, J. H. Cafarella, R. W. Ralston, and E. Stern, "Convolvers for DPSK Demodulation of Spread Spectrum Signals," in 1976 Ultrasonics Symposium Proceedings (IEEE, New York, 1976), pp. 451-455, DDC AD-A040519/1.
3. K. L. Wang, "Modal Analysis of SAW Convolver" (unpublished).
4. G. I. Stegeman, IEEE Trans. Sonics Ultrason. SU-23, 33 (1976).
5. R. Joly, "Design of a Convolver for Optical Imaging," E. L. Ginzton Laboratory Report No. 2560, Stanford University (May 1976).
6. Solid State Research Report, Lincoln Laboratory, M.I.T. (1977:2), pp. 55-60, DDC AD-A044795.
7. R. W. Ralston, J. H. Cafarella, S. A. Reible, and E. Stern, "Improved Acoustoelectric Schottky-Diode/LiNbO₃ Memory Correlator," in 1977 Ultrasonics Symposium Proceedings (IEEE, New York, 1977) (to be published).
8. F. J. Leonberger, J. H. Cafarella, R. W. Ralston, E. Stern, and A. L. McWhorter, "Acoustoelectrically Scanned Gap-Coupled Si-Diode Array/LiNbO₃ Imaging Devices," in 1977 Ultrasonics Symposium Proceedings (IEEE, New York, 1977) (to be published).

UNCLASSIFIED

SECURITY CLASSIFICATION OF THIS PAGE (When Data Entered)

REPORT DOCUMENTATION PAGE		READ INSTRUCTIONS BEFORE COMPLETING FORM
1. REPORT NUMBER ESD-TR-77-294	2. GOVT ACCESSION NO.	3. RECIPIENT'S CATALOG NUMBER
4. TITLE (and Subtitle) Solid State Research		5. TYPE OF REPORT & PERIOD COVERED Quarterly Technical Summary 1 August - 31 October 1977
		6. PERFORMING ORG. REPORT NUMBER 1977:4
7. AUTHOR(s) Alan L. McWhorter		8. CONTRACT OR GRANT NUMBER(s) F19628-78-C-0002
9. PERFORMING ORGANIZATION NAME AND ADDRESS Lincoln Laboratory, M.I.T. P.O. Box 73 Lexington, MA 02173		10. PROGRAM ELEMENT, PROJECT, TASK AREA & WORK UNIT NUMBERS Program Element No. 65705F Project No. 649L
11. CONTROLLING OFFICE NAME AND ADDRESS Air Force Systems Command, USAF Andrews AFB Washington, DC 20331		12. REPORT DATE 15 November 1977
		13. NUMBER OF PAGES 76
14. MONITORING AGENCY NAME & ADDRESS (if different from Controlling Office) Electronic Systems Division Hanscom AFB Bedford, MA 01731		15. SECURITY CLASS. (of this report) Unclassified
		15a. DECLASSIFICATION DOWNGRADING SCHEDULE
16. DISTRIBUTION STATEMENT (of this Report) Approved for public release; distribution unlimited.		
17. DISTRIBUTION STATEMENT (of the abstract entered in Block 20, if different from Report)		
18. SUPPLEMENTARY NOTES None		
19. KEY WORDS (Continue on reverse side if necessary and identify by block number)		
solid state devices	photodiode devices	infrared imaging
quantum electronics	lasers	surface-wave transducers
materials research	laser spectroscopy	charge-coupled devices
microelectronics	imaging arrays	acoustoelectric devices
surface-wave technology		
20. ABSTRACT (Continue on reverse side if necessary and identify by block number)		
<p>This report covers in detail the solid state research work of the Solid State Division at Lincoln Laboratory for the period 1 August through 31 October 1977. The topics covered are Solid State Device Research, Quantum Electronics, Materials Research, Microelectronics, and Surface-Wave Technology. Funding is primarily provided by the Air Force, with additional support provided by the Army, ARPA, NSF, and DOE.</p>		

DD FORM 1 JAN 73 1473 EDITION OF 1 NOV 65 IS OBSOLETE

UNCLASSIFIED